

TOPICAL REVIEW

# LISA technology and instrumentation

**O Jennrich**<sup>1</sup>

ESA/ESTEC, Keplerlaan 1, 2200 AG Noordwijk, The Netherlands

E-mail: [oliver.jennrich@esa.int](mailto:oliver.jennrich@esa.int)

**Abstract.** This article reviews the present status of the technology and instrumentation for the joint ESA/NASA gravitational wave detector LISA. It briefly describes the measurement principle and the mission architecture including the resulting sensitivity before focussing on a description of the main payload items, such as the interferometric measurement system, comprising the optical system with the optical bench and the telescope, the laser system, and the phase measurement system; and the disturbance reduction system with the inertial sensor, the charge control system, and the micropropulsion system. The article touches upon the requirements for the different subsystems that need to be fulfilled to obtain the overall sensitivity.

PACS numbers: 04.80.Nn ,95.55.Ym ,07.87.+v ,07.60.Ly

Submitted to: *Class. Quantum Grav.*

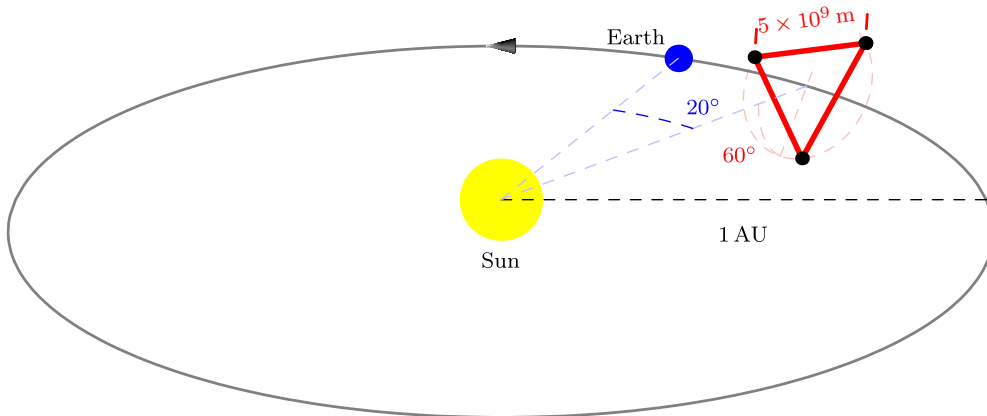


**Figure 1.** Schematics of the LISA constellation orbiting the Sun. The constellation is inclined by  $60^\circ$  with respect to the ecliptic and trails the Earth by about  $20^\circ$ , resulting in a distance of about  $50 \times 10^6 \text{ km}$  to Earth. The distance between the satellites (the armlength) is nominally  $5 \times 10^6 \text{ km}$ .

## 1. Introduction

LISA is a space mission, jointly planned by ESA and NASA with the purpose to detect and observe low frequency gravitational waves [1–4]. In contrast to ground-based gravitational wave detectors [5–11] that have a typical sensitivity in the range from 1 Hz to 1 kHz, the sensitivity for LISA stretches between 0.1 mHz and 0.1 Hz, accessing a frequency window that is inaccessible to ground-based detectors due to seismic noise and gravity gradient noise.

The sensitivity for low frequencies allows LISA to assess gravitational waves that are emitted by some of the most violent events in the Universe, such as the coalescence of massive black holes ( $m_{\text{BH}} \approx 10^5 M_\odot \dots 10^7 M_\odot$ ). Other sources include the capture of stellar-size compact objects by massive black holes and the signal from binary systems in our galaxy. The science of LISA is discussed in detail in [12–18] and is beyond the scope of this paper.

### 1.1. Mission concept

LISA comprises three spacecraft in a heliocentric orbit, forming an equilateral triangle with  $5 \times 10^6 \text{ km}$  a side (the “armlength” of the constellation), inclined by  $60^\circ$  with respect to the ecliptic and trailing the Earth by about  $20^\circ$  (see figure 1). Basic orbital mechanics [19] cause the constellation to maintain its size and shape closely for the nominal duration of the mission, allowing to operate LISA without further station keeping manoeuvres. However, tidal forces on the constellation cause the distances between the satellites to change by up to 1%, resulting in a differential velocity along the line of sight of up to 15 m/s and in slight change of the constellation’s shape (figure 5). The distance toward the Earth, approximately  $5 \times 10^7 \text{ km}$ , has been chosen as a compromise between long-term stability of the constellation and communications requirements.

To reach the operational orbits, the three spacecraft are provided with propulsion modules that will allow manoeuvring during the 14 month cruise phase and the final

orbit insertion, after which the propulsion modules will be jettisoned.

The nominal mission life is 5 years, the launch is currently foreseen in the 2020 timeframe.

As gravitational waves cause a strain in the space-time [20], measuring the change in the distance of spatially separated objects is a common concept for measuring the effect of gravitational waves. Each spacecraft houses two test masses, kept as close as possible in free fall, that form the reference points for an interferometric measurement of the inter-spacecraft distance.

The ability to keep the test masses in near geodesic motion, the required control law, aspects of the interferometry, and the  $\mu\text{N}$ -thrusters as well as the operational aspects of such a mission will be demonstrated in the LISA Pathfinder mission, a technology precursor to LISA that is foreseen to launch in 2011. LISA Pathfinder will put two test masses in a near-perfect gravitational free fall, and control and measure their motion with an accuracy that is only factors of a few less than required for LISA. While the hardware of LISA pathfinder has been designed with the LISA performance in mind, in order to save on testing and verification, the requirements on the acceleration noise for LISA Pathfinder and the lower end of the frequency band are about a factor of 10 relaxed compared to LISA.

A full description of LISA Pathfinder is beyond the scope of this paper and the reader is referred to [21, 22] and references therein.

### 1.2. Sensitivity

The interferometric measurement allows to assess the distance between the (almost) free-falling test masses to a level of  $10 \text{ pm}/\sqrt{\text{Hz}}$ , resulting in a strain sensitivity of about  $10^{-20}/\sqrt{\text{Hz}}$ , enough to detect, e. g. the coalescence of massive black holes even at redshifts of  $z = 20$  with a signal-to-noise-ratio of several hundreds [17, 23, 24]. The science requirements for LISA define the sensitivity in a frequency window from  $3 \times 10^{-5} \text{ Hz}$  to  $0.1 \text{ Hz}$  (figure 2) as this is where most of the sources for LISA are expected to emit.

The limitation to the sensitivity at frequencies below approximately 3 mHz is given by residual acceleration noise of the order of  $3 \times 10^{-15} \text{ m/s}^2$  acting on the test masses. At higher frequencies, the noise associated with the position measurement limits the sensitivity to about  $10 \text{ pm}/\sqrt{\text{Hz}}$ . The sensitivity is further reduced for frequencies above about 30 mHz by the transfer function of the detector: the effect of gravitational waves starts to cancel out as soon as the wavelength of the gravitational wave approaches an integer multiple of the optical path in the detector [25].

The sensitivity of LISA to changes in the distance between the spacecraft is low, compared with ground-based detectors. However, as gravitational waves produce a *strain*, or a fractional change in distance, the large distance between the satellites provides a sensitivity to gravitational waves comparable to those of the much shorter ground based detectors.

### 1.3. Measurement principle

For practical reasons, the interferometric measurement in LISA is broken up into three distinct parts: the measurement between the spacecraft, i. e. between the optical benches that are fixed to the spacecraft, and the measurement between each of the test masses and its respective optical bench (see figure 4). Such a partition of the

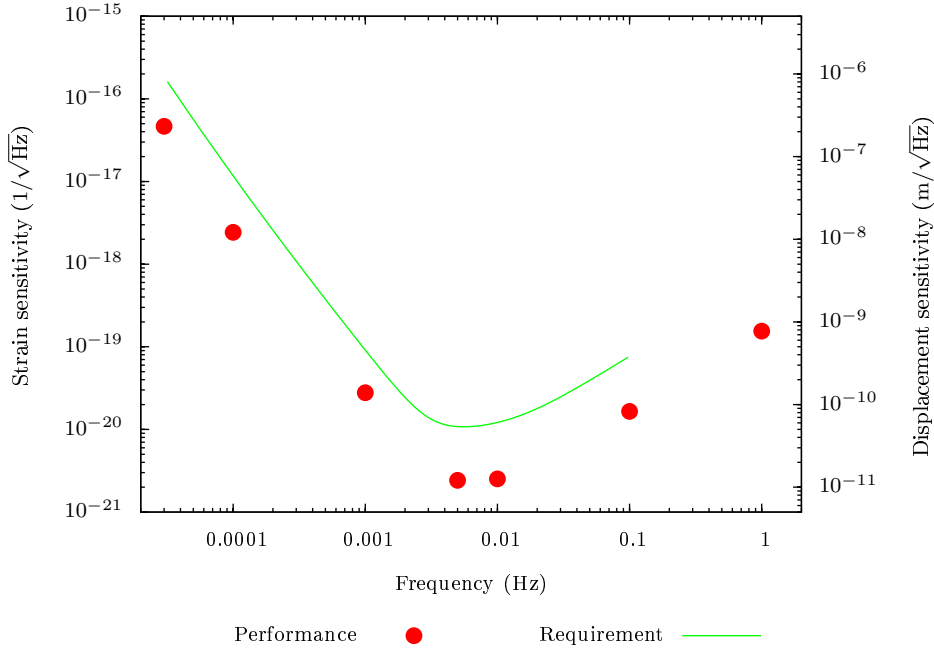


**Figure 2.** Sensitivity requirements (green solid) and current best estimate of the performance (red dots). The strain sensitivity (left axis) is given for the full instrument, the displacement sensitivity (right axis) has been converted to a *single arm* link, i.e. represents the equivalent accuracy for the armlength measurement, combining all noise sources. The design of the instrument is such that a  $\sim 35\%$  performance margin is included, resulting in the values for the current best estimate to be consistently lower than the requirement.

measurement would be normally avoided, as it multiplies the detection noise. However, as the noise budget for LISA is dominated by the contribution of the shot noise in the measurement between the spacecraft, this technique only contributes a negligible amount of noise.

The distance between the test mass and the optical bench is measured by reflecting light off the proof mass and combining this measurement beam with a local oscillator on the optical bench (“test mass interferometer”).

To measure the distance between the spacecraft, about 2 W of infrared light (1064 nm) is sent through a 40 cm telescope, used for receiving and transmitting, to the respective far spacecraft, i.e. spacecraft A transmits to spacecraft B and C (nomenclature as in figure 3) *etc.*, forming six single laser links. In an ordinary interferometer, the received light would be directly reflected back to the transmitting spacecraft A where the light would be combined with a local oscillator, completing the measurement. However, due to the large distance between the two spacecraft, a direct reflection of the light is not feasible. Diffraction widens the transmitted laser beam to many kilometres at the receiving spacecraft and the received power is of the order of 100 pW (or about  $5 \times 10^8$  photons per second), resulting in a dilution factor of  $10^{-10}$ .

Therefore, a transponder scheme with offset phase-locking is implemented. The

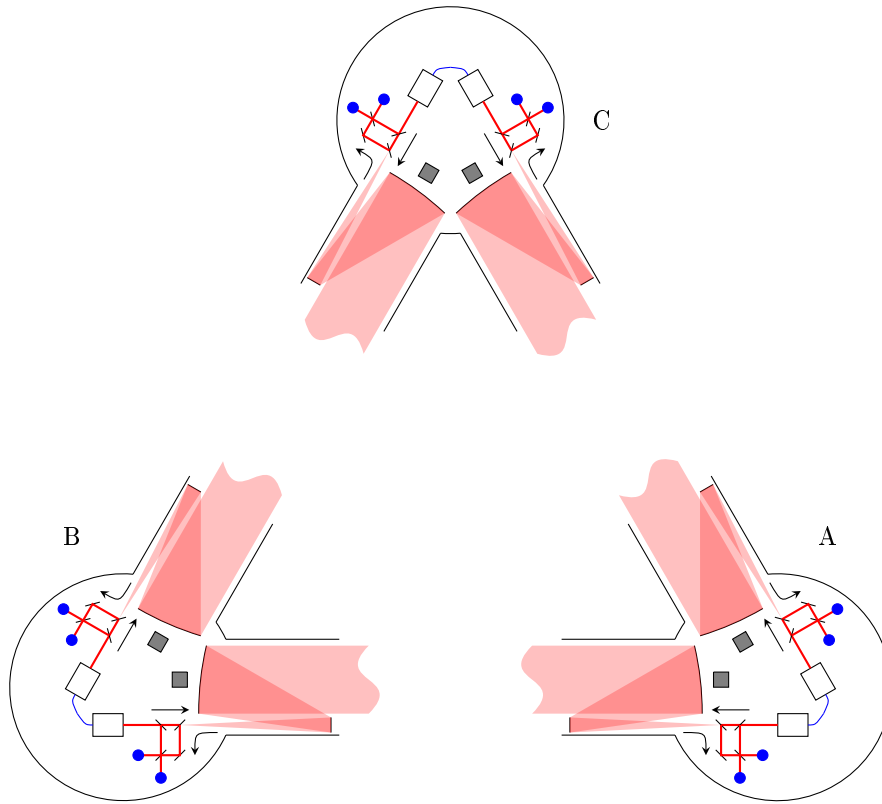


**Figure 3.** Schematics of the laser links in the LISA constellation. Each satellite transmits laser light to the two other satellites and receives laser light from the two other satellites. The laser used for transmitting is phase-locked to the received laser light, establishing a transponder scheme. As transmitted and received light share the same telescope, a polarisation multiplexing scheme is used to separate the two beams. The use of linear polarisations requires slightly different optical benches on the sending and the receiving spacecraft. The blue (solid) dots indicate where the interferometric measurements are taken. Proof masses are shown in grey; the interferometry to determine their position has been left out for clarity.

received light on spacecraft B is combined with a local oscillator derived from the transmitting laser (B) and the phase difference is measured. The frequency of the laser (B) can then be controlled so that the beat note corresponds to an electronic offset frequency. This way, the phase of the transmitting laser can be made to be a true copy of the phase of the received light. Recombining the light on spacecraft A then yields a beat note that contains the electronic offset frequency, the Doppler shift (that can be as large as 15 m/s) and the signal due to the gravitational wave (“science interferometer”). To be able to distinguish a gravitational wave signal from a noise in the electronic offset frequency, the latter needs to be known precisely enough. This is achieved by multiplying the clock frequency on each spacecraft up to a few GHz and transferring them via sidebands to the other spacecraft where the sidebands can be compared to the local clock, thus allowing to assess the clock noise and to correct for it.

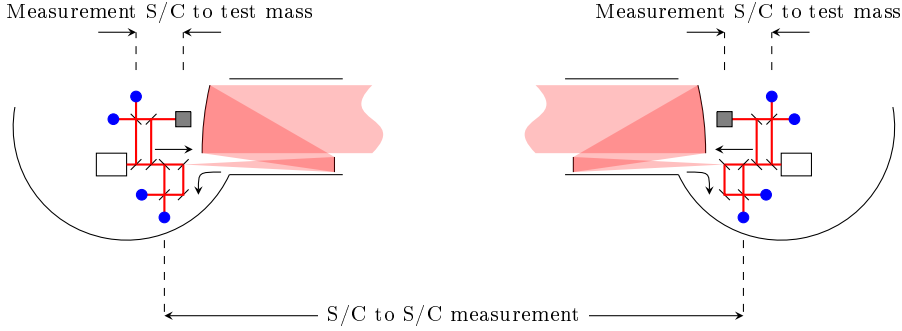


**Figure 4.** Partition of the LISA measurement. Each measurement between two test masses is broken up into three different measurements: two between the respective test mass and the spacecraft and one between the two spacecraft. As the noise in the measurement is dominated by the shot noise in the S/C-S/C measurement, the noise penalty for the partitioning of the measurement is negligible. The blue (solid) dots indicate where the interferometric measurements are taken.

Extending the phase-locking scheme to include a phase-locked loop (PLL) between the two lasers on one spacecraft, it is obvious that all six lasers can be phase-locked to one (arbitrarily chosen) master laser. Such a scheme requires of 9 individual phase measurements, two for each arm and one each between the two lasers on a single spacecraft. In addition each measurement of the test masses with respect to the optical bench requires another 6 phase measurements, so that a total of 15 phase measurements carry the complete information on the gravitational waves.

## 2. Optical system

The optical system of LISA contains all the optical components and their support that are needed for the interferometry. More specifically, each spacecraft comprises one *optical assembly* (figure 6, lower row) that consists of two units each (figure 6, upper row), each made up from the *optical bench*, the *telescope*, and the *gravitational reference sensor* as well as the associated mounting structures.

The optical bench is mounted parallel to the primary mirror of the telescope, requiring a non-planar beam path, where the light from the optical bench to the telescope has to be directed “up” to the telescope.

The Gravitational Reference Sensor (GRS) is mounted behind the optical bench so that the light from the optical bench to the GRS has to pass through the optical bench (“down”), resulting in a non-planar beam path as well.

### 2.1. Optical bench

The required functionality of the optical bench (figure 7) causes a relatively complex optical bench (figure 8).

The primary laser (2W at end of life, see section 3) provides the light to be sent to the far spacecraft, the reference beam for the science interferometer, and the measurement beam to the local interferometer, the reference interferometer and the metrology for the point-ahead mechanism (PAAM, see sec. 2.1.3). A small portion of

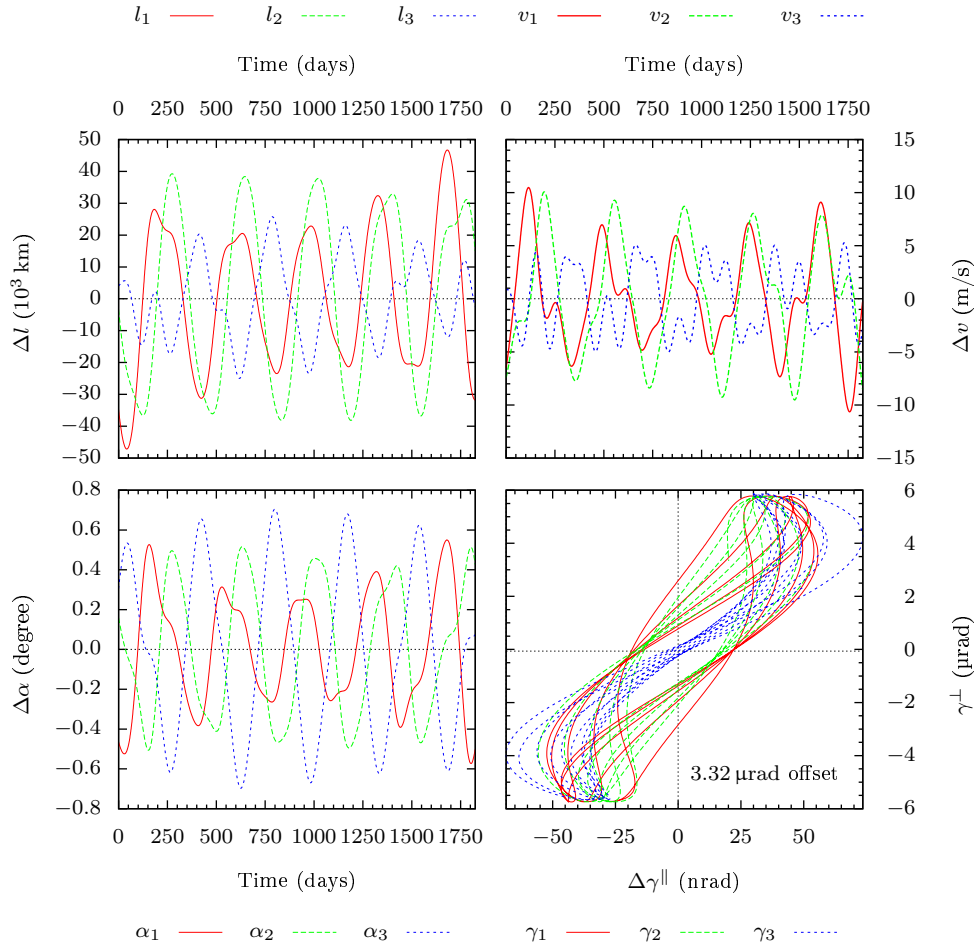


**Figure 5.** Time evolution of the LISA constellation for a five year mission duration. Upper left: Time variation  $\Delta l$  of the armlengths of the constellation. The variation is limited to about  $\pm 1\%$  of the armlength, i. e.  $\pm 50 \times 10^6$  m. Upper right: relative velocities  $\Delta v$  between the spacecraft in line-of-sight, limited to  $\pm 15$  m/s. For the chosen laser wavelength (1064 nm), 1 m/s corresponds to 1 MHz Doppler shift. Lower left: Variation of the inner angles of the constellation around the nominal value of  $60^\circ$ , limited to  $\pm 0.8^\circ$ . Lower right: Point-ahead angle for the three spacecraft for a nominal orbit. The out-of-plane angle  $\gamma^\perp$  shows a negligible offset with a variation of  $\pm 6 \mu$ rad that needs to be corrected for the outgoing beam, whereas the in-plane angle  $\gamma^\parallel$  displays a large constant offset of about  $3.32 \mu$ rad and a small and negligible variation of about 100 nrad.

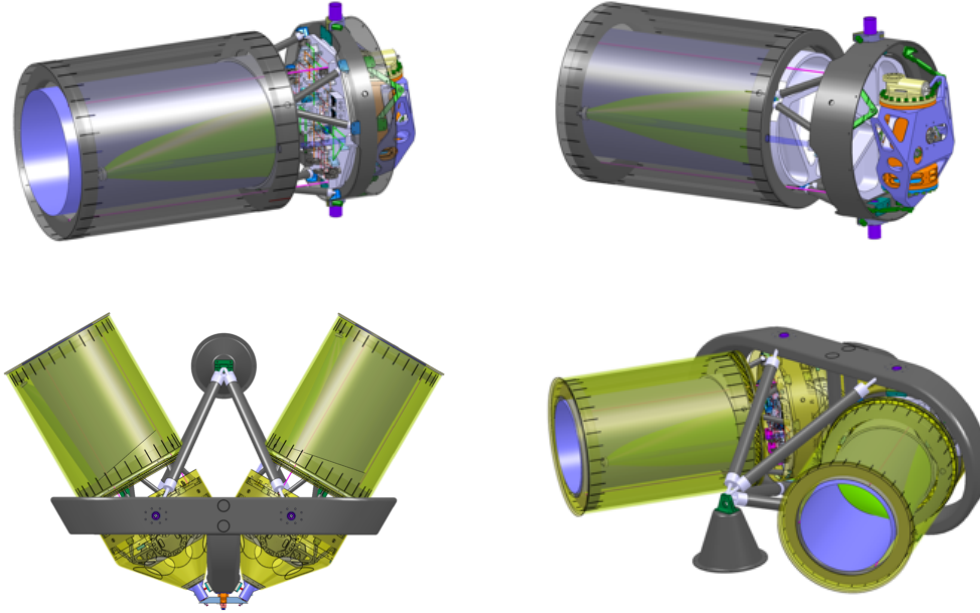


**Figure 6.** Optical assembly. Telescope with optical bench attached (upper row). The optical bench is orthogonal to the telescope axis with the optical components facing the main mirror of the telescope (upper left). The inertial sensor is attached behind the optical bench (upper right) to a support ring also holding the optical bench. A support structure takes the two sub-units (lower row), forming the optical assembly. The angle between the two telescopes is nominally 60 degrees, but can be adjusted within  $\pm 1.5^\circ$ .

the primary laser’s light is directly send to a laser power monitor so that the output power of the laser can be measured and controlled.

The secondary (100 mW) laser serves as reference beam to the interferometers used in the PAAM metrology, the measurement of the position of the test mass, the reference interferometer and the optical truss.

Both, primary and secondary laser are delivered to the optical bench through single-mode, polarisation maintaining optical fibres. The polarisation is fixed by a polariser on the optical bench.

Each spacecraft carries two optical benches, so instead of providing two independent lasers per bench, each bench’s primary laser serves as the other bench’s secondary laser. For that, a portion of the light of the primary laser is brought to the other optical bench through a fibre that connects the two optical benches (“backside fibre link”).

*2.1.1. Interferometric measurement techniques* The interferometric measurements in LISA are based on heterodyne interferometry, where two laser with respective frequencies  $\nu_0$  and  $\nu_0 + \Delta\nu$  are combined to yield a beat note with the frequency  $\Delta\nu$ , the phase of which is then detected.

Measurements of longitudinal displacements can be performed by directing the combined light on a single element photo detector, whereas for the measurements of angular displacements, *differential wavefront sensing* [26] is needed. Here, the light is

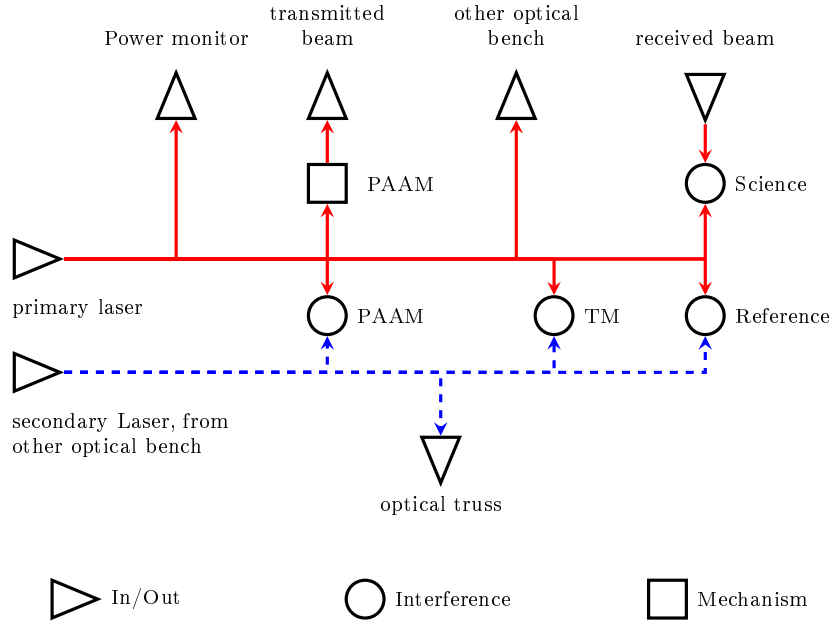


**Figure 7.** Functional diagram of the optical bench. Light from the primary laser (red, solid line) is directed to the power monitor, transmitted to the telescope via the point-ahead mechanism (PAAM), and is used for interferometric measurements of the PAAM, the test mass (TM) and the reference interferometer as well as for interfering with the received light (Science). The secondary laser (blue, dashed line) provides light to the optical truss and the interferometric measurements.

directed on to a quadrant photo detector (QPD) and the differential phase between the signals from the different quadrants is used to determine the angle of the wavefront arriving at the photodiode. In practise, taking the sum of QPD’s signal is used to emulate a single element photo detector so that one interferometer can measure both angular displacement and longitudinal displacement simultaneously.

All the interferometers on the optical bench are read out by two photodetectors, one in each output of the interferometer, providing redundancy and an increase of the signal-to-noise ratio by a factor of  $\sqrt{2}$  in the nominal case (i. e. with both detectors working).

**2.1.2. Science Interferometer** The science interferometer measures the distance between the receiving and the transmitting optical bench on two spacecraft.

Most of the primary laser’s light passes through a beam expander necessary to match the beamsizes on the optical bench (5 mm) to the telescope, followed by an aperture stop and the point-ahead-mechanism (see section 2.1.3) before encountering first a polarising beamsplitter set for reflection, and then the telescope “back optics” (see section 2.2) before encountering the telescope and been sent out to the receiving spacecraft.

One of the two benches involved in transmitting and receiving the light carries additionally a half-wave plate in the path of the transmitted light, resulting in orthogonal polarisations for the beams in different directions (figure 3), so that

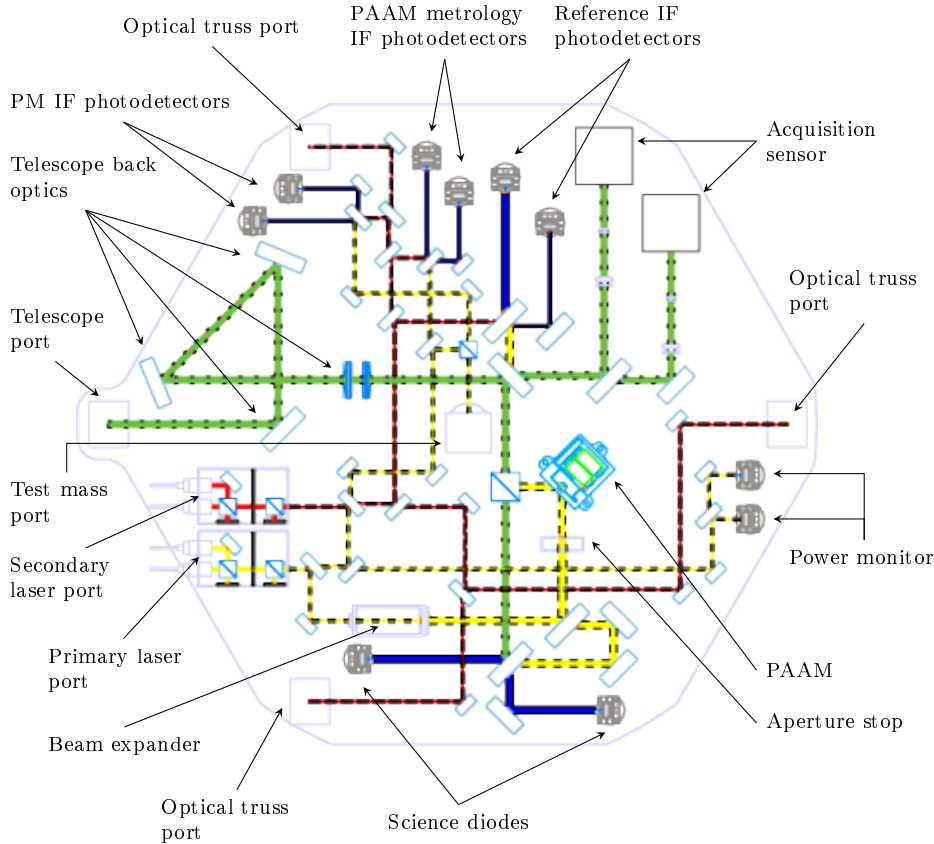


**Figure 8.** Present baseline architecture for the optical bench. The light received from the telescope is depicted green (short dash), the light from the primary and secondary laser is depicted yellow (normal dash) and red (long dash), respectively. Interfering beams are depicted blue (solid line). The optical bench carries the telescope back optics, acquisition sensors, the point-ahead mechanism (PAAM) and all the optics and detectors needed for the interferometry. Beams to the test mass, the optical truss and the telescope are orthogonal to the optical bench and enter and exit through the respective ports. The width of the beams indicates the physical beam diameter.

transmitted and received beam can be separated by means of a polarising beamsplitter.

As the primary laser provides the reference beam for the science interferometer as well, part of the light is split off after the beam expander and its polarisation rotated by 90 degrees through another half-wave plate to match the polarisation of the reference beam to that of the received beam.

The light received from the far spacecraft ( $\approx 100\text{ pW}$ ) enters through the telescope and the telescope port onto the optical bench and is directed from the telescope back optics directly to the science interferometer where it is combined with the reference beam (figure 10, upper left). As the light passes a half wave plate either on transmission or on reception (but never on both), the received beam is now polarised orthogonally to the transmitted beam (see figure 3). Therefore, the polarising beamsplitter used to reflect the transmitted beam to the telescope back

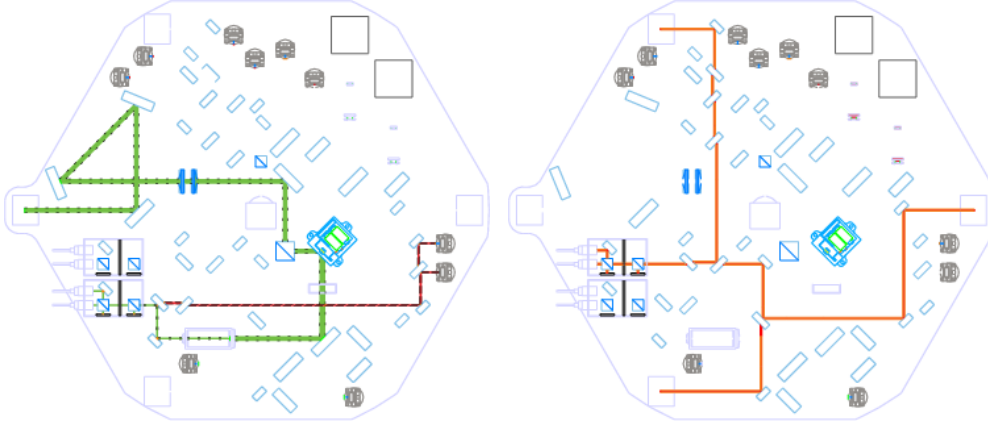


**Figure 9.** Non-interferometric beam paths on the optical bench. The drawing on the left shows the outgoing beam (green, short dash) and the light directed to the power monitors (red, long dash) coming from the primary laser. The drawing schematics on the right shows the beams coming from the secondary laser going to the optical truss ports.

**Table 1.** Requirements on the point-ahead mechanism (PAAM).

	Requirement
Dynamical range	$\pm 700 \mu\text{rad}$
Optical path-length stability	$3 \frac{\text{pm}}{\sqrt{\text{Hz}}} \times \sqrt{1 + \left(\frac{3 \text{mHz}}{f}\right)^4}$
Angular stability	$16 \frac{\text{nrad}}{\sqrt{\text{Hz}}} \times \sqrt{1 + \left(\frac{3 \text{mHz}}{f}\right)^4}$

optics transmits the received light.

While the optical benches are designed as identical as possible, the polarisation multiplexing scheme causes a slight difference, as one of the benches on a spacecraft will have a half wave-plate in the transmit/receive path where the other doesn't.

**2.1.3. Point-ahead angle mechanism** The point ahead mechanism (PAAM) compensates the aberration for the beam transmitted to the far spacecraft (see figure 9). The aberration, the angle between the received and transmitted light, is due to the fact that the velocity of the far spacecraft has a component perpendicular to the line of sight, i. e. the far spacecraft appears to move sideways. This component changes amplitude and direction over the course of time, causing a time varying aberration. Any constant aberration could be taken out by a pre-launch alignment process, however, the variation in the aberration makes an on-orbit mechanism necessary as a varying angle between the measurement beam and the local oscillator degrades the contrast on the photo detectors.

The aberration can be decomposed into two components, projected into the plane of the constellation and perpendicular to that. Most of the constant aberration of about  $3.32 \mu\text{rad}$  is in the plane of the constellation, most of the variation (but very little offset) is perpendicular to the plane of constellation and amounts to about  $\pm 6 \mu\text{rad}$

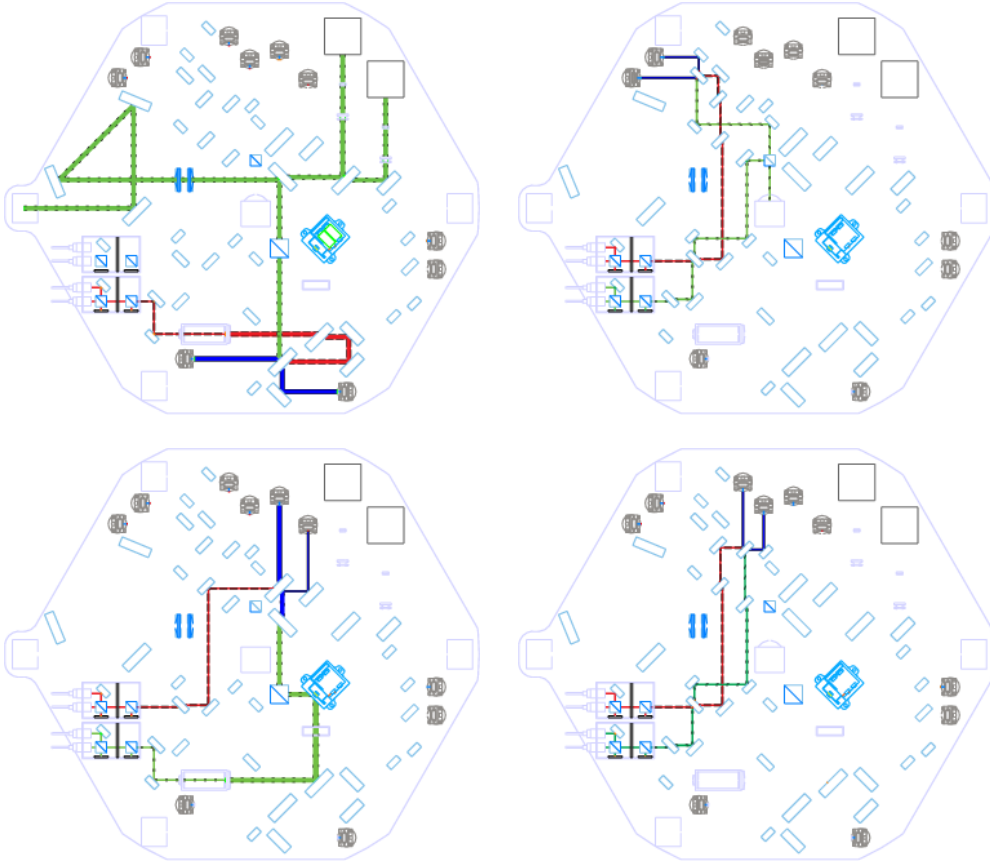


**Figure 10.** Interferometric beam paths on the optical bench. Reference and measurement beams are always shown in green (short dash) and red (long dash), respectively. Beam paths after the recombining beamsplitter are depicted in blue (solid line). Upper left, the main science interferometer is shown with light going to the acquisition sensors positioned in the upper right of the optical bench, the upper right shows the test mass interferometry. On the lower left the metrology interferometer for the point-ahead mechanism (PAAM) is shown and the lower right depicts the reference interferometer.

(figure 5). The in-plane offset is taken care of by pre-launch alignment and the in-plane variation is small enough to not cause discernible loss of contrast. The out-of-plane component, however, requires on-orbit correction. It is worthwhile noting that due to the fact that the optical bench itself is perpendicular to the plane of the constellation, the out-of-plane angle  $\gamma^\perp$  actually lies in the plane of the optical bench, so that the correction keeps the optical path planar.

As the aberration depends only on the orbital dynamics of the constellation, it can be predicted with high accuracy and the necessary commands for the point-ahead angle mechanism can be uploaded to the spacecraft well in advance, so that no closed-loop controller is foreseen. However, should it be necessary, such a closed loop controller can be implemented by evaluating the wavefront at the receiving spacecraft and the orientation of both sending and receiving spacecraft.

Situated on the optical bench, the PAAM is exposed to the full magnification

of the telescope ( $\times 80$ ), so that the range of the point-ahead mechanism needs to be  $\pm 480 \mu\text{rad}$  for the nominal case,  $\pm 700 \mu\text{rad}$ , including margin. Furthermore, the point-ahead mechanism is unavoidably in the optical path of the science interferometer, so it has to fulfil stringent requirements on the path-length noise it introduces; the optical path-length noise has to be smaller than  $3 \text{ pm}/\sqrt{\text{Hz}}$  for frequencies above 3 mHz. The angular jitter noise of the mechanism is required to be smaller than  $16 \text{ nrad}/\sqrt{\text{Hz}}$  for frequencies above 3 mHz. Here, the telescope magnification works in favour of a less stringent requirement, as the angular jitter of the transmitted beam is reduced by the telescope magnification.

The point-ahead angle and the optical path-length error are monitored through dedicated metrology on the optical bench (figure 10, lower left), allowing to implement a local control of the PAAM.

The currently developed solutions for the PAAM both depend on monolithic designs (Haberland hinge [27] and bending flexures, respectively) that have no freely rotating axis but translate elastic deformation of thin blades into a rotation. This allows to achieve very little friction and hysteresis for the rotation while keeping a high stiffness in the other degrees of freedom.

*2.1.4. Test Mass Interferometer* The test mass interferometer is used to determine the position of the test mass of the gravitational reference sensor with respect to the optical bench. Together with the science interferometer, the test mass interferometer on the transmitting and the receiving optical bench can be combined to perform the measurement of the distance between the free-falling proof masses, i. e. the test mass interferometer provide an integral part of the science measurement.

The reference beam for this interferometer is taken from the secondary laser, the measurement beam comes from the primary laser. The measurement beam is directed through the optical bench to the test mass situated in the gravitational reference sensor at the backside of the optical bench. The test mass acts as a mirror and reflects the measurement beam back the optical bench. Similar to the science interferometer, the measurement beam is out of the plane of the optical bench (figure 10, upper right).

Separation of the beam going to the test mass and the reflected beam is again done through polarisation, which is different from the setup used in LTP that relies on a geometrical separation of the two beams [26]. In LISA, an additional quarter-wave plate is therefore needed that is passed twice by the light, effectively resulting in a rotation of the polarisation by  $90^\circ$ . Another half-wave plate rotates the polarisation of the measurement beam back by  $90^\circ$  to coincide with the polarisation of the reference beam and allow interference.

The test mass interferometer provides information on both longitudinal movement of the test mass with respect to the optical bench (and hence the spacecraft) and rotation through differential wavefront sensing. The readout of the test mass interferometer will therefore be used to feed into the control law of the disturbance reduction system, augmenting the signals from the capacitive readout (see section 5)

*2.1.5. Optical truss* The optical truss interferometry is a method to assess the stability of the telescope structure (see section 2.2) on orbit. It consists of three pick-off mirrors separated by  $120^\circ$  on the mounting structure for the secondary mirror of the telescope, that use a sample of the outgoing light for a measurement beam. Beamsplitter and photo detector are co-located with the sampling mirror, the reference

beam is taken from the secondary laser (figure 9, right). Taking the measurements at three points allows to reconstruct the shape of the wavefront of the outgoing light as it is needed for diagnosis and correction in post-processing.

*2.1.6. Reference Interferometer* The reference interferometer provides information on the frequency noise of the primary laser with respect to the secondary laser. Taking its measurement beam from the primary laser and its reference beam from the secondary laser, it is deliberately designed to have unequal optical path-lengths for the interfering beams so that the relative frequency noise of primary and secondary laser can be assessed (figure 10, lower right).

The output signal of the reference interferometer is used to provide an error signal for the phase-locking of the primary and the secondary laser.

*2.1.7. Optical bench construction* The optical bench is constructed much alike the optical bench for the LISA Technology Package (LTP) experiment on board LISA Pathfinder [28–30], with Zerodur as a material for the bench and fused silica for most of the optical components. Hydroxy-catalysis bonding is used to attach the optical components to the optical bench. This technology, first developed for the use in the GP-B mission [31, 32], has found broad applications as well in ground-based gravitational wave detectors [33, 34] as e. g. in LISA Pathfinder [35] due to its excellent properties regarding dimensional stability of the components and rigidity and durability of the bond itself.

While Zerodur has the advantage of a very low coefficient of thermal expansion (CTE) of about  $2 \times 10^{-8}$ , it is quite brittle and care has to be taken to restrict the mechanical load on the bench by an appropriate design of the surrounding structure. The necessary expertise has been developed during the construction of the optical bench for LTP.

The few differences between the construction of the optical bench for LISA with respect to the optical bench for LPF lie in the use of polarising components for LISA, requiring mounting technology for different materials, as polarisers are usually not made from fused silica, and in the inclusion of mechanisms on the optical bench such as the point-ahead actuator.

## 2.2. Telescope

The telescope baselined for LISA is an off-axis telescope with a 40 cm aperture, a mechanical length of about 60 cm, and a field of view of  $\pm 7 \mu\text{rad}$  out-of-plane and  $\pm 4 \mu\text{rad}$  in plane in which the most stringent wavefront requirements have to be met. The choice of an off-axis telescope was driven by the stringent requirement on stray light that is hard to achieve with a secondary mirror in normal incidence. Additionally, the off-axis design has the advantage of not blocking part of the incoming light, thus allowing more light for the measurement process.

The size of the telescope’s aperture is determined by the amount of laser power required for a given sensitivity, as the size of the aperture determines both the widening of the beam due to diffraction and the amount of laser power collected from the received beam. A diameter of 40 cm results in an equivalent pathlength noise due to shot-noise of about  $8 \text{ pm}/\sqrt{\text{Hz}}$ , the dominating contribution to the noise budget at frequencies above 3 mHz.

**Table 2.** Main requirements on the telescope. The full field of view is required for acquisition. The wavefront quality is required only for the smaller field of view in the science mode.

	Requirement
Aperture	40 cm
Total field of view	400 $\mu$ rad full angle
science mode	$\pm 7 \mu$ rad out-of-plane $\pm 4.2 \mu$ rad in-plane
Optical pathlength stability	$1 \frac{\text{pm}}{\sqrt{\text{Hz}}} \times \sqrt{1 + \left(\frac{3 \text{ mHz}}{f}\right)^4}$
Magnification	80
Wavefront quality	$\frac{\lambda}{30}$ for $Z_2$ and $Z_3$ and the root square sum of $Z_5$ and higher.

With a magnification of the telescope of 80 and a diameter of the outgoing beam of 400 mm, the input beam to the telescope has a diameter of 5 mm. A beam expander, situated on the optical bench (figure 8), matches the typical beam diameter on the optical bench (1 mm) to the diameter required by the telescope.

As equally important as the telescope’s ability to gather light is the quality of the wavefront leaving the telescope. An ideal, perfectly spherical wavefront with its centre at the position of the test mass would render the measurement of the optical pathlength insensitive to any pointing jitter of the sending spacecraft, as all the radii of a sphere have the same length. Any deviation from such an ideal wavefront, however, will translate a spacecraft jitter into an equivalent pathlength noise.

The point spread function (PSF) that is customarily used to define the optical quality of a telescope is of limited use for the LISA telescope. On the one hand, not all the wavefront distortions that contribute to the PSF are of importance for LISA, on the other hand, the PSF does not provide enough information on the distortions that are relevant for LISA.

The requirements for the wavefront distortion are therefore specified, somewhat unusual, in terms of the amplitudes of Zernike polynomials with a root mean square value of less than  $\lambda/30$  for  $Z_2$  and  $Z_3$  each, corresponding to a tilted waveform in the far-field, and a total of  $\lambda/30$  for the root square sum of all other Zernike polynomials  $Z_5$  and higher over the whole field of view.

As the wavefront errors critically depend on the position of the beam waist with respect to the telescope, the telescope can be refocused on orbit by adjusting the position of two lenses in the telescope “back-optics”.

Additionally, the back-optics image the exit pupil of the telescope to the centre of the test mass, the photodetectors of the science interferometers and the point-ahead mechanism, minimising the effect of spacecraft rotation on the science measurement.

An additional complication arises from the fact that the telescopes for LISA form part of the interferometric path of the science interferometer, i. e. any change in optical pathlength between e. g., the primary and secondary mirror, directly contributes to noise degrading the science signal. To reduce the impact of any geometrical distortions, the optical truss interferometry (see section 2.1.5) can be used to directly measure the wavefront of the outgoing beam for later correction in post-processing.

### 2.3. Optical assembly tracking mechanism

In addition to the time variation of the angle between the received and the transmitted light that is caused by the aberration, the angle between the two telescopes on board one spacecraft changes over time as well. Nominally  $60^\circ$ , it varies by about  $1.5^\circ$  over the course of a year due to orbital mechanics (figure 5). To compensate for that variation, a mechanism that changes the angle between the two telescopes is required, the so-called *optical assembly tracking mechanism* (OATM), as can be seen in the lower left of figure 6, connecting the rear ends of the two single assemblies.

The OATM acts upon the complete assembly of gravitational reference sensor, optical bench and telescope, rotating the assembly around an axis perpendicular to the plane of the constellation. This way, the OATM is *not* part of the optical path of an interferometer, therefore requiring much less care with regard to introducing translations in addition to rotations.

The requirements on angular jitter are similar to the residual spacecraft jitter, i. e. on the order of a few  $\text{nrad}/\sqrt{\text{Hz}}$ .

## 3. Laser system

The laser system currently baselined for LISA makes use of the Master Oscillator Fibre Power Amplifier (MOFPA) approach [36, 37]. For LISA, the low power master oscillator is largely identical to the laser used by the LTP experiment on board LISA pathfinder [21], a Nd:YAG non-planar ring oscillator (NPRO) pumped by an internally redundant, fibre-coupled arrangement of laser diodes. The LTP laser is manufactured by Tesat GmbH [38], emitting 30 mW of 1064 nm light and has been used in a similar configuration on board the TerraSAR-X satellite [39, 40].

The light of the NPRO passes an optical isolator to suppress optical feedback and is coupled into two optical single-mode fibres, the smaller fraction of the light is taken to be used for prestabilisation purposes, the larger fraction fed into a fibre-based electro-optical modulator, that imprints sidebands used for clock-transfer and ranging. From there, it enters a double-clad fibre amplifier, pumped by a redundant array of fibre-coupled laser diodes, bringing the laser power up to the required 2 W. After passing another optical isolator and an on/off switch controlled by the spacecraft computer, the light is then delivered via an optical fibre directly to the optical bench (figure 11)

As polarisation encoding is used in LISA to distinguish transmitted from received light, the light entering the optical bench needs to be linearly polarised. This is ensured by a polariser as the first component on the optical bench. To avoid unnecessary stray-light, 98 % of the light power arriving on the optical bench needs to be in the linear polarisation transmitted by the polariser.

As the position of the test masses is read out interferometrically in the test mass interferometry, the requirement on the permissible acceleration noise for the test masses leads to a requirement on the power stability of the laser, as a variation in laser power causes a variation in radiation pressure on the test masses and therefore a variation in the acceleration. Consequently, the intensity noise for the laser has to be smaller than  $1 \text{ mW}/\sqrt{\text{Hz}}$  at 3 mHz. A summary of the requirements on the laser at end-of-life is given in table 3.

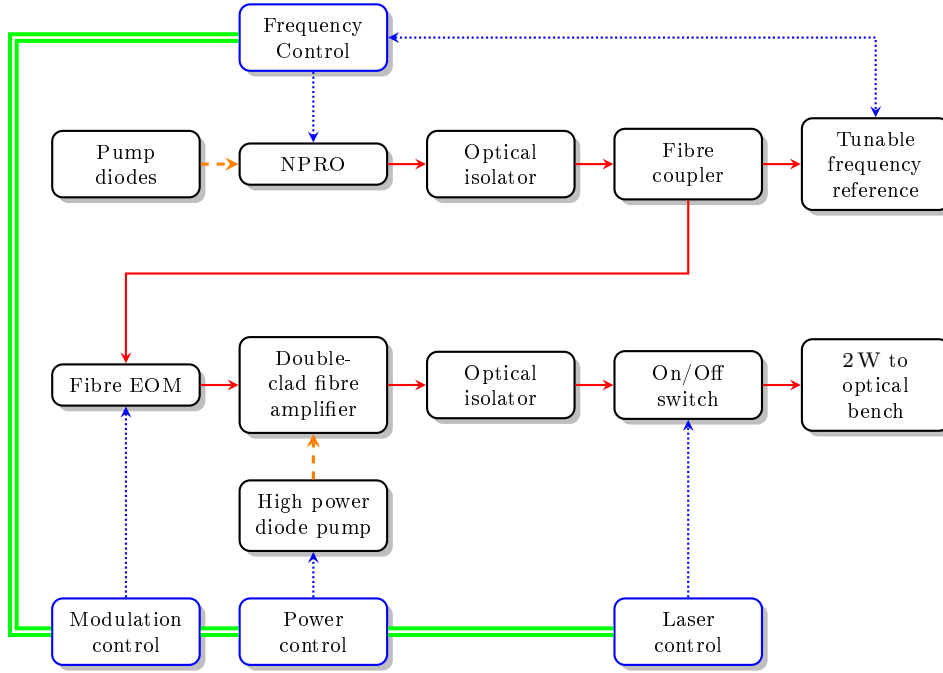


**Figure 11.** Schematics of the LISA laser system. Laser light is denoted by the red lines (solid), starting from the NPRO laser via the electro-optic modulator (EOM) to the fibre amplifier on to the optical bench. The pump light is shown orange (dashed). Control inputs are denoted with blue lines (dotted), the spacecraft bus connecting the control units in green (double line).

**Table 3.** Laser requirements, specified at end-of-life.

	Requirement
Wavelength	1064.5 nm
Output power	2 W
Polarisation	linear, containing more than 98 % of optical power in main polarisation
Power stability	$1 \frac{\text{mW}}{\sqrt{\text{Hz}}} \times \sqrt{1 + \left(\frac{3 \text{ mHz}}{f}\right)^4}$

### 3.1. Laser Frequency noise suppression

Frequency stabilisation of the lasers is a vital part of the LISA measurement scheme. As in any interferometric length measurement, a frequency noise  $\delta\nu$  causes an equivalent noise in the length measurement  $\delta x$  that is proportional to the difference of optical pathlength  $\Delta L$  and the fractional frequency noise.

$$\delta x = \Delta L \frac{\delta\nu}{\nu} \quad (1)$$

The difference in optical pathlength in LISA can be as large as  $\Delta L = 10^8$  m due to the orbital motion of the spacecraft and the equivalent pathlength noise contribution

**Table 4.** Frequency stabilisation requirements

Stabilisation stage	Performance after stabilisation in $\frac{\text{Hz}}{\sqrt{\text{Hz}}}$
Free running	$\frac{10^4 \text{ Hz}}{f}$
Pre-stabilisation	$\frac{30 \text{ Hz}}{f} \times \sqrt{1 + \left(\frac{3 \text{ mHz}}{f}\right)^4}$
Arm locking	$0.3 \times \sqrt{1 + \left(\frac{3 \text{ mHz}}{f}\right)^4}$
TDI	$4 \times 10^{-7} \times \sqrt{1 + \left(\frac{3 \text{ mHz}}{f}\right)^4}$

allocated to frequency noise is around  $\delta\tilde{x} = 0.4 \text{ pm}/\sqrt{\text{Hz}}$  at 3 mHz. This results in a required frequency stability of  $\delta\tilde{\nu} = 1.2 \times 10^{-6} \text{ Hz}/\sqrt{\text{Hz}}$  at 3 mHz. Starting from a free-running laser that has a typical frequency noise of  $\delta\tilde{\nu}_{\text{free}} = 3 \text{ MHz}/\sqrt{\text{Hz}}$  at 3 mHz, such a reduction of frequency noise by about 12 orders of magnitude is difficult to achieve in a single step.

Therefore, a three level approach has been chosen for LISA. First, a pre-stabilisation of the free-running laser to a level of  $30 \text{ Hz}/\sqrt{\text{Hz}}$ , then a stabilisation of the laser to the LISA arms and finally the post-processing stage as a last step.

*3.1.1. Prestabilisation* The prestabilisation is the first stage of the frequency stabilisation scheme for LISA. It requires a local frequency reference, such as a cavity [41–43], a molecular resonance [44, 45] or a dedicated heterodyne interferometer with unequal arms (much like the one employed in the LISA Pathfinder experiment [46, 47])

Laser stabilisation to a cavity using a variety of techniques, most prominently RF-sideband locking has been demonstrated to well beyond the required stability for LISA (see e. g. [48] for a demonstration of a stability of  $\delta\tilde{\nu} = 1 \text{ Hz}/\sqrt{\text{Hz}}$  for frequencies above 1 Hz) at frequencies somewhat higher than the LISA frequency band. In the LISA frequency band, thermally driven changes of the cavity length are a major contributor to the residual frequency noise. As the thermal environment for LISA will be exceptionally stable, this is mainly a problem for laboratory-based demonstration or verification experiments, as those need sophisticated thermal insulation to reach the required stability. Using multiple-stage insulation systems, a frequency stability of  $\tilde{\nu} = 30 \text{ Hz}/\sqrt{\text{Hz}}$  at 3 mHz has been demonstrated at NASA’s Goddard Space Flight Center (GSFC) [43]. The cavities used in this experiment underwent environmental testing and the given performance has been reached before and after the testing cycle.

The stabilisation of a frequency-doubled Nd:YAG laser to a hyperfine absorption line of the  $\text{I}_2$  molecule has a long history as well. Typically used for comparing absolute frequencies in metrology, ([49, 50]), iodine stabilisation has been employed in ground-based gravitational wave detectors [51] and is currently under investigation for applications in LISA [44, 45, 52]. where frequency stability of around  $10 \dots 100 \text{ Hz}/\sqrt{\text{Hz}}$  in the frequency range of  $1 \dots 100 \text{ mHz}$  has been demonstrated in tabletop experiments [45, 51].

In contrast to the stabilisation on a cavity resonance, stabilisation on a molecular line provides an absolute frequency reference; the drawback is some added complexity

due to the need of frequency-doubled light. Recently, a frequency-doubling system has been qualified for space application in the framework of the technology development for the SIM mission [53], greatly reducing the impact of frequency doubling on the technology development for LISA.

Heterodyne interferometry, as opposed to the “homodyne” stabilisation schemes described above, does not require a tuning of the laser to the reference, as it provides an error signal largely independent of the common-mode frequency of the light used. The drawbacks are the need for two light fields, separated by the heterodyne frequency and the comparatively low sensitivity. The use of a heterodyne interferometer with optical paths deliberately chosen to be unequal has been proposed for LISA, using a scheme much alike the the reference interferometer in the LTP experiment on board LPF.

*3.1.2. Arm-locking* A possible second stage of the frequency stabilisation scheme uses the interferometer arms of LISA as a frequency reference. By design, the fractional stability of the arms in the frequency range of around 1 mHz is on the order of  $\delta\tilde{x}/L \sim 10^{-21}/\sqrt{\text{Hz}}$  and is guaranteed to fulfil the science requirements for LISA.

Arm-locking therefore makes use of this stability and derives an error signal from the phase-difference of the local laser and the received light. As the received light is phase-locked to the local laser at the remote spacecraft, it can be regarded to carry a replicate of the noise of the local laser delayed by one full round-trip time  $\tau = 33\text{ s}$  [54]. After choosing a suitable control law, the noise is suppressed at frequencies  $f$  smaller than the corresponding round-trip frequency  $f_0 = 1/\tau = 30\text{ mHz}$  but causes significant amplification of the noise at integer multiples of  $f_0$  [55] as well as a long decay time for the initial conditions. A more elaborate implementation of arm-locking [56] uses the phase-differences from both arms in sum and difference to suppress the noise spiking.

The main advantage of the arm-locking scheme is the additional suppression of the laser frequency noise without the need of any additional hardware, as the sensors for the required phase measurements and the actuators for setting the laser frequency are already present. The control law is fully implemented in software and requires no additional resources.

A proof-of-concept implementation in hardware use RF signals instead of light and a 300 m coaxial cable to simulate the LISA arm [57] and shows the feasibility of unity gain frequencies above the inverse of the delay time ( $\tau = 1.6\ \mu\text{s}$  as well as the predicted amplification of the noise and the “ringing” after lock acquisition. Similar experiment, using light in optical fibres ( $L = 10\text{ km}$ ,  $\tau = 100\ \mu\text{s}$ ) and purely electronical delays [58] yield comparable results.

*3.1.3. Time delay interferometry* The third stage of the frequency stabilisation scheme, time-delay interferometry (TDI), does not reduce the laser frequency noise *in situ*, but rather suppresses the effects of laser frequency noise in a post-processing stage. In contrast to standard interferometers, where the light from the two arms is combined optically and the phase of the individual light impinging on the recombining beamsplitter is not known, in LISA each incoming light is combined optically with a reference beam individually, so that the phase of the incoming light is individually measured and recorded. This allows to make use of correlations in the frequency noise and to remove the frequency noise down to the level of the measurement accuracy

provided for the individual phase measurements by algebraically combining phase measurements data delayed by multiples of the distance between the spacecraft to the so called *TDI variables*.

It must be pointed out, that the ability to use the individual phase measurements in post-processing does *not* depend on the actual values of the measurements. This means that TDI is not in any way restricted by arm-locking (or does in any way restrict arm-locking, for that matter) [59].

The first implementation of the algorithm was based in the frequency domain and dealt with a much simplified constellation [60]. Such a frequency-domain based implementation is difficult to generalise to the case of changing arm-length differences and more complex interferometric schemes.

Subsequent implementations of the algorithm have therefore been based in the time-domain and include signals from all three spacecraft [61, 62]. The simple time-domain implementation of the TDI algorithm (“first generation TDI”) using only phase measurement data delayed by the respective distances between the spacecraft only cancels the frequency noise exactly for fixed inter-spacecraft distances (much like the algorithm in the frequency domain) and requires a initial frequency noise of the lasers not larger than  $5 \text{ Hz}/\sqrt{\text{Hz}}$  [63]. Further refinements of the algorithm (“second generation TDI”) allow to deal with changing arm-lengths as well [64, 65] by using phase measurements data that are delayed by multiples of the inter-spacecraft distances.

Using TDI with changing arm-lengths requires in addition the ability to perform phase measurements at arbitrary times to accommodate for the fact that the travel time of the light between the spacecraft will not only be different for each arm, but also changing over time. This additional complication can be overcome by oversampling and subsequent high-precision interpolation [59] of the phase measurements.

A rigorous algebraic approach to the mathematics of TDI progressed as well from considering a purely static constellation [66] to coping with changing arm-lengths [67] and a fully relativistic treatment of the optical links [68]. The set of TDI variables forms a complete set of interferometric observables, so that any interferometric combination can be retrieved by linearly combining suitable TDI variables [66]. Furthermore, suitably chosen linear combinations of TDI variables correspond to optimal statistical inference [69].

A review of the current state-of-the art techniques and the mathematical understanding of the algorithm can be found in [70].

*Experimental demonstration* A full experimental demonstration of TDI is difficult to achieve, mainly because of the need to provide sufficient, or at least representative, time delays between the data streams. As using a propagation delay through free space is clearly out of the question, all experimental approaches use electronic delays of the measured signal to emulate the optical delay. Using this techniques, experimental demonstrations of the TDI with a delay of 2 s and later 16 s [71, 72] showed a reduction of the laser phase noise by 5 orders of magnitude at around 1 mHz, coming close to the required LISA performance.

#### 4. Phase measurement

The phasemeter for LISA is one of the few payload items that can claim no or very little heritage from LISA Pathfinder. The main reason lies with the fact that LISA

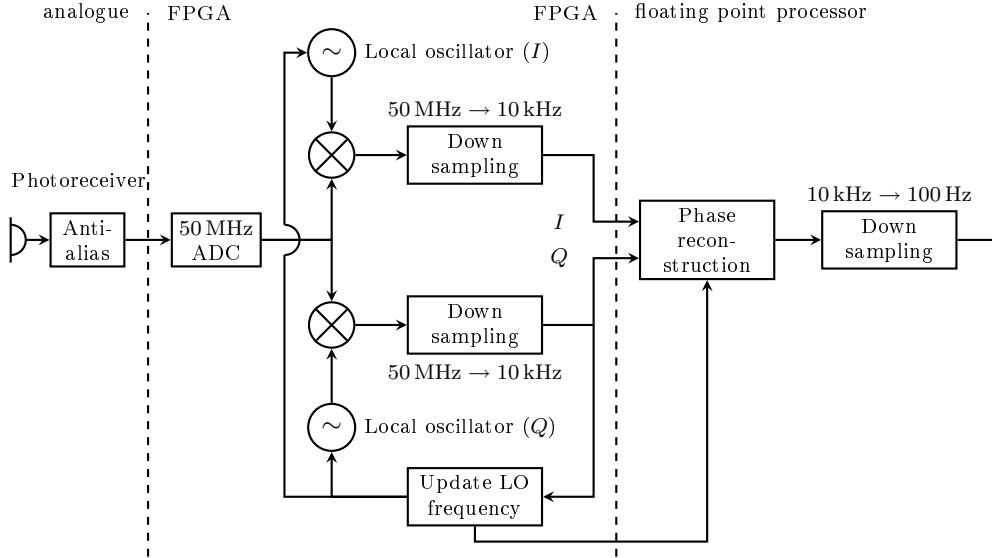


**Figure 12.** Block diagram of the LISA phasemeter. Signals from the photodetector pass an analogue anti-alias filter before digitisation in an 50 MHz analogue-digital converter (ADC) and further processing to determine phase and frequency, based on integer arithmetic in a field programmable gate array (FPGA). A phase reconstruction algorithm to correct residual tracking errors is implemented in a floating point processor and feeds back to the local oscillator.

Pathfinder uses a relatively low heterodyne frequency of about 1.6 kHz [26, 73] in its interferometers, the heterodyne frequency for LISA is much higher due to the relative motion of the spacecraft and the resulting Doppler effect. The requirement for the LISA phasemeter calls for a maximum admissible frequency heterodyne frequency of 15 MHz and for a frequency rate of up to 1 Hz/s. Additionally, the phasemeter must be compatible with data transfer and ranging tones on the laser link between the spacecraft as well as with the transmission of the clock signal, none of which are present on LISA Pathfinder.

One way to address the challenge of measuring the phase of a heterodyne signal at around 10 MHz is by a counting and timing technique, where the integer numbers of cycles in a longer time period (e. g. 10 ms corresponding to 100 Hz measurement frequency) are counted and the remaining fraction of a cycle is measured by a high precision timer. Such a scheme has been demonstrated [74, 75] and proven to be compatible with data transfer between spacecraft [76].

The phasemeter architecture baselined for LISA is based on a more traditional digital phase locked loop (DPLL) as sketched in figure 12. The signal from the photoreceiver passes through an analogue anti-alias filter and is then digitised at 50 MHz on an 8 bit analogue-digital-converter (ADC). The digitization frequency has to be chosen high enough to exceed the Nyquist frequency for the highest occurring beat note in the system.

The signal is then multiplied with a local oscillator whose frequency is close to the signal frequency. The down-sampled, i. e. low-pass filtered and decimated, output of this multiplication is directly proportional to the *phase* difference between signal

and local oscillator and is used as an error signal to drive the frequency and phase of the local oscillator to be the same as for the signal. The DPLL operates at 10 kHz, updating the local oscillator every 0.1 ms, fast enough to follow the frequency changes occurring in LISA. For performance reasons, these operations are implemented in a field programmable gate array (FPGA) and all operations are based on integer arithmetic.

Residual tracking errors are corrected by evaluating the information in the two quadratures of the error signal in a floating point processor and combine those with the local oscillator phase. Further filtering of the signal yields the output at a rate of 100 Hz for recording. A more detailed insight into the principle of operation of the phasemeter including initial results on simulated data is given in [77].

## 5. Disturbance Reduction System

The disturbance reduction system (DRS) of LISA is one of the main components of the mission. Whereas the interferometric measurement system allows to measure the distance between the test masses to picometer accuracy, the DRS is responsible to render these measurements meaningful, as it ensures that the test masses follow as much as possible gravitational orbits, i. e. experience as small as possible accelerations.

Thus the DRS consists of the gravitational reference sensor and its ancillary structures, the micro-Newton propulsion system that is used to provide the thrust for the fine attitude and position control of the spacecraft, and the control law that takes the data from the gravitational reference sensor and controls the micro-Newton thrusters such as to keep the spacecraft centred on the test mass.

### 5.1. Principle of operation

The DRS main objective is to maintain the free fall of a test mass that serves as nominal reference point for the measurement of the inter-spacecraft distance. To keep the test mass in free fall, the DRS measures the position and orientation of the test mass with respect to the spacecraft, applies a control law and commands micro-newton thrusters so that the test mass remains in its nominal position with respect to the spacecraft.

Situated inside the spacecraft, the test mass is shielded from the external effects, such as solar radiation pressure and (to a certain degree) the interplanetary magnetic field. In addition, the spacecraft architecture has to ensure that the forces on the test mass are as small as possible, requiring special design precautions regarding the mass distribution, the thermal balance and the magnetic cleanliness.

Each spacecraft has two gravitational reference sensors (GRS), each mounted in the line of sight of the corresponding telescope (see figure 6, upper right panel), behind the optical bench. The *sensitive axis* of the DRS denotes the axis aligned to the line of sight to the telescope and consequently to the test mass in the remote spacecraft (see figure 13). As LISA employs two test masses per spacecraft, it is impossible to keep both of them in free fall condition in all degrees of freedom and ensure at the same time that the test masses stay close to their nominal position. However, it is sufficient to maintain free fall in the direction of the sensitive axes which can be achieved by controlling the “non-sensitive” degrees of freedom of the test masses and the position and attitude of the spacecraft. The measurement of the test mass position is provided

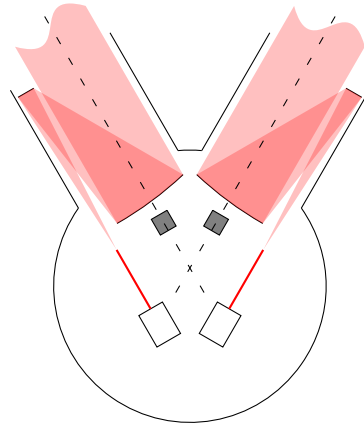


**Figure 13.** Position and orientation of the two test masses (dark grey) in the spacecraft. The sensitive axes of the sensors are indicated with the dashed lines and are aligned with the direction to the far spacecraft.

by a capacitive readout system, augmented in the sensitive axes by the measurement provided by the test mass interferometer.

The DRS can claim substantial heritage from LISA Pathfinder, as the gravitational reference sensor will be identical and the micro-Newton thrusters and the control law will be similar, requiring adaptation to the larger mass of the LISA spacecraft and the different geometry of the test mass arrangement. Similarly, lifetime requirements for the propulsion system are more stringent as LISA's nominal life-time is 5 years compared to the 6 month of LISA Pathfinder.

### 5.2. Environmental requirements

As gravitational forces cannot be shielded, the mass distribution of the spacecraft can cause significant acceleration on the test mass, both through direct gravitation as well as through gravity gradients.

To be able to compensate both mass imbalance and gravity gradient, the mass distribution on the spacecraft has to be known accurately enough to be able to use the correct amount of compensation mass in the correct position. On ground, a measurement of the self-gravity is not feasible to the precision necessary for LISA, verification of the self-gravity relies on analyses. Such analyses on self-gravity and the design of compensation masses has been successfully performed on LISA Pathfinder [78, 79] and the corresponding analysis tools have been developed for LISA [80, 81].

Of similar importance is the magnetic cleanliness of the spacecraft, as magnetic fields can cause a non-gravitational acceleration of the test mass coupling to its non-zero magnetic susceptibility. In addition, they create an acceleration noise as soon as the test mass carries an electric charge. As neither the magnetic susceptibility of the test mass nor its electric charge can be controlled to be precisely zero, strict magnetic cleanliness has to be enacted, requiring the use of non-magnetic materials in the vicinity of the inertial sensor.

Temperature fluctuations at the inertial sensor have the potential to cause acceleration noise, as they will cause a time varying gas pressure in the electrode

housing leading to varying radiometer effect. The thermal variations allowed are at the level of  $10^{-5} \text{ K}/\sqrt{\text{Hz}}$

### 5.3. Gravitational Reference Sensor

The gravitational reference sensor (GRS) forms a crucial part of the LISA mission and is one of the major components of the disturbance reduction system, providing it with the data necessary to keep the spacecraft in a (nearly) gravitational orbit.

The GRS comprises the test mass (figure 14, upper left), enclosed in a housing (figure 14, upper right) that contains the electrodes needed for the capacitive readout of the test mass position. The electrodes are arranged in such a way that all relevant degrees of freedom can be capacitively measured [82–84]. The GRS further contains the launch lock mechanism (figure 14, lower row) and the charge control system.

Forcing of the test mass to control its orientation and position in the non-sensitive directions is achieved by applying AC voltages to the electrodes; the unavoidable cross-coupling of the actuation from non-sensitive directions into the sensitive directions has to be as small as possible (on the order of  $10^{-3}$ ) to avoid “leakage” into the sensitive axis that causes acceleration noise of the test mass. Knowledge of the correct cross-coupling coefficients and an effective diagonalisation of the control matrix is an important task during on-orbit commissioning of the instrument.

Other important noise sources in the GRS to consider comprise the electrostatic coupling between the test mass and the housing (and ultimately the spacecraft) due to the capacitive sensing, the *stiffness* of the sensor, that feeds the the noise of the micro-newton thrusters back into the GRS [85]; forces induced by thermal gradients, such as thermal radiation pressure, or asymmetric outgassing [86]; random charging processes [87, 88]; and gas damping.

The patch field effect, caused by spatial (and temporal) variation of the work function, can be a major source of noise to drag-free sensors [89]. The work function of the test mass contributes to stray DC electrostatic fields that couple to the time-varying charge of the surrounding electrode housing (and vice versa), introducing both forcing and sensing noise.

A technique to measure the stray DC field imbalances has been proposed [90] and experimentally verified [83] that simulates a sinusoidally varying charge on the test mass by applying a dither voltage to selected electrodes. Using this method, the average bias voltage that results from the spatial variation of the work function can be suppressed by a factor of about 100 by applying a DC compensation voltage, resulting in a reduction of the respective acceleration noise to levels negligible for LISA.

The GRS is a direct heritage from the LTP experiment on LISA Pathfinder; a detailed review on the working principle of the GRS can be found in [91]. An extensive ground-testing campaign evaluating the performance and the noise sources on in the GRS employing a low-frequency torsion pendulum is under way and results and more detailed descriptions of noise sources and their effect can be found in [83, 85, 92, 93]; requirements on the sensor and the environmental conditions are summarised in table 5.

**5.3.1. Test mass and housing** The test mass is a cube made of an alloy of about 75 % Au and 25 % Pt with a mass of 1.96 kg and dimension  $46 \text{ mm} \times 46 \text{ mm} \times 46 \text{ mm}$ .

The mixing ratio of the two metals is chosen so that the magnetic susceptibility  $\chi$  can be made very small [94, 95]. As the susceptibility depends on the mixing ratio and

**Table 5.** Summary of the environmental and performance requirements on the DRS.

Condition	Requirement
Acceleration	
DC	$3 \times 10^{-9} \text{ m s}^{-2}$
residual variation	$3 \times 10^{-15} \text{ m}/(\text{s}^2 \sqrt{\text{Hz}})$
Capacitive readout noise	
Displacement (sensitive axis)	$1.8 \text{ nm} \sqrt{\text{Hz}}^{-1}$
Displacement (non-sensitive axis)	$3.0 \text{ nm} \sqrt{\text{Hz}}^{-1}$
Rotation	$200 \text{ nrad} \sqrt{\text{Hz}}^{-1}$
Forcing noise	
Sensitive axis	$2 \times 10^{-15} \text{ m s}^{-2} \sqrt{\text{Hz}}^{-1}$
Non-sensitive axes	$3 \times 10^{-14} \text{ m s}^{-2} \sqrt{\text{Hz}}^{-1}$
Rotation	$7.3 \times 10^{-13} \text{ rad s}^{-2} \sqrt{\text{Hz}}^{-1}$
Thermal variation across the sensor	$10^{-5} \text{ K}/\sqrt{\text{Hz}}$
Magnetic field	
DC field	$4 \times 10^{-6} \text{ T}$
DC gradient	$10^{-6} \text{ T m}^{-1}$
Variation	$72 \times 10^{-9} \text{ T} \sqrt{\text{Hz}}^{-1}$
Variation of gradient	$25 \times 10^{-9} \text{ T m}^{-1} \sqrt{\text{Hz}}^{-1}$
Charge on test mass	$10^7$ electron charge
Absolute position of Test mass inside electrode housing	$1.5 \times 10^{-9} \text{ m}/\sqrt{\text{Hz}} \times \sqrt{1 + \left(\frac{8 \text{ mHz}}{f}\right)^4}$

the manufacturing process, a small residual magnetic susceptibility of  $\chi \approx -2 \times 10^{-5}$  remains in the test mass, requiring a certain amount of magnetic cleanliness of the whole spacecraft that prohibits the use of ferro-magnetic materials in the vicinity of the GRS.

The surface of the test mass is coated with a thin layer of gold that provides reflectivity for the laser light of the local interferometer. In addition gold proves to be the material of choice to minimise the patch field effect.

The test mass is surrounded by a housing that contains the electrodes for the capacitive sensing and actuating. The housing is slightly larger than the test mass, with the gap between the test mass and the electrodes measures between 3 mm and 4 mm provides a further reduction of the patch field effect, as the noise forces decrease with the distance between test mass and electrodes. An additional benefit of the large gaps is a reduction of the dissipation due to gas flow around the test mass.

The electrode housing admits the the fingers and the plunger of the launch lock and repositioning mechanism (see section 5.3.3) in the  $Z$  surfaces and the laser of the test mass interferometer through a hole in the  $X$  surface.

The electrodes are made from a gold-coated sapphire substrate, surrounded by a molybdenum guard ring; the electrode housing structure is made from molybdenum as well.

The physical properties of test mass and housing are summarised in table 6.

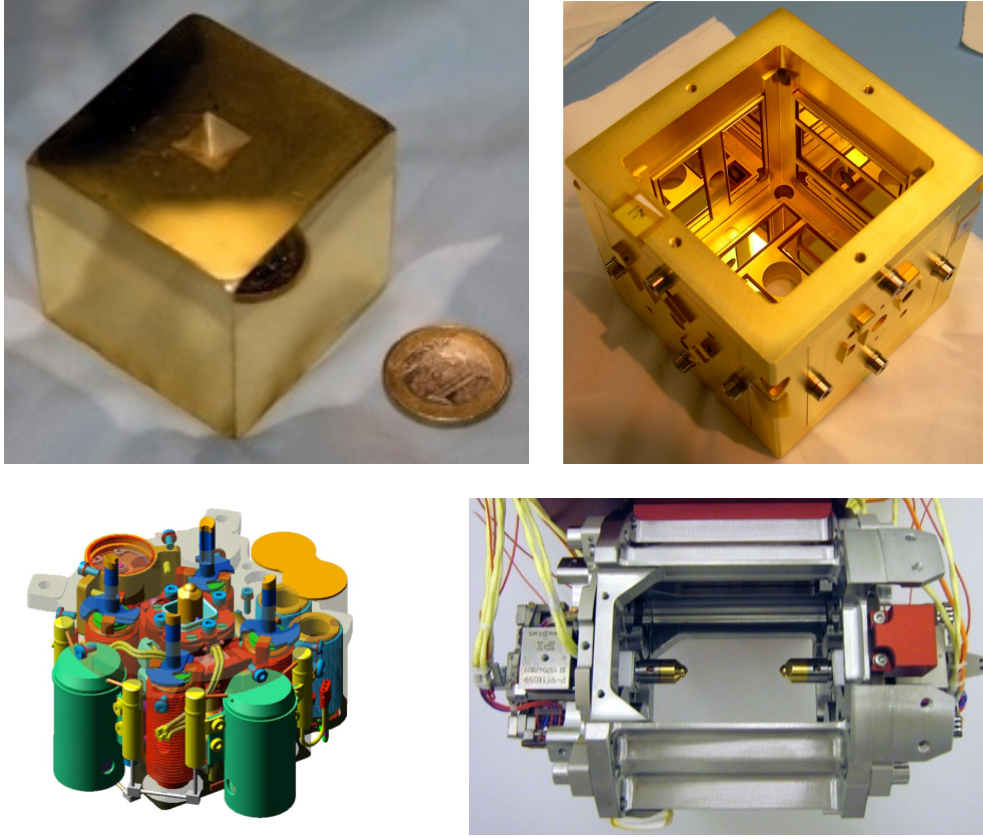


**Figure 14.** Upper left: LISA Pathfinder test mass made of a metallic mixture of 75% gold and 25% platinum, coated with gold. The prism-like impression at the centre of the top face takes the plunger of the caging system and allows for centring of the test mass, the chamfered corners accept the fingers during launch lock. Edges are chamfered to prevent damage during caging. Upper Right: Electrode Housing. Lower left: Schematic drawing of the bottom half of the caging mechanism, with the central plunger in the centre and the four hydraulically actuated fingers that grab onto the corners of the test mass. Lower right: Flight model of the caging mechanism (side view, courtesy of Thales Alenia Space) with both plungers visible.

*5.3.2. Capacitive sensing* The capacitive sensing of the test mass position is designed to minimise the disturbance of the test mass while at the same time yielding a measurement with noise levels of  $1.8 \text{ nm}/\sqrt{\text{Hz}}$  for the sensitive axis. Six opposing pairs of electrodes form a differential capacitive-inductive bridge with a resonance frequency of about  $\omega_0 = 2\pi \times 100 \text{ kHz}$ . Combinations of the obtained signals yield all displacements and rotations. In order to apply the AC bias to the test mass, injection electrodes are placed on the  $+Z$  and  $-Z$  as well as on the  $+Y$  and  $-Y$  surfaces of the electrode housing (figure 16). The capacitive sensing achieves a sensitivity of  $2 \text{ nm}/\sqrt{\text{Hz}}$  in displacement and  $200 \text{ nrad}/\sqrt{\text{Hz}}$  in rotation [96] in ground tests, matching or exceeding the requirements for LISA.

The details of the sensor design and a detailed discussion of the noise can be found in [97].

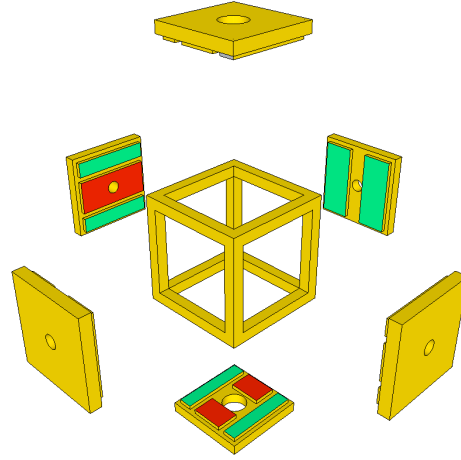


**Figure 15.** Exploded schematic view of the electrode housing, showing the structure of the electrode housing and the electrodes mounted on the inner faces.

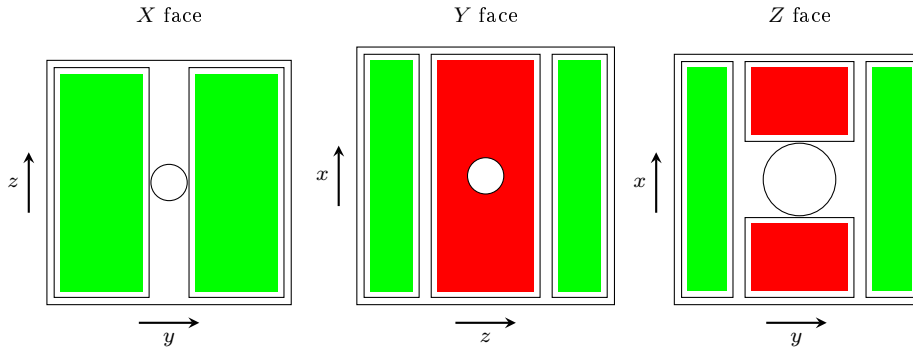


**Figure 16.** Placement of the electrodes onto the inner surfaces of the electrode housing. Control electrodes are given in green (light grey), injection electrodes in red (dark grey). The central holes in the X- and Y-faces admit the laser, the central hole in the Z face admits the plunger. The electrodes differ slightly in overall size on the different faces.

**Table 6.** Summary of the physical parameters of the test mass and the housing.

Element	Property
Test mass	
Size	46 mm × 46 mm × 46 mm
Material	gold-coated AuPt (75 % Au, 25 % Pt )
Mass	1.96 kg
Magnetic susceptibility	$ \chi  \leq 2 \times 10^{-5}$
Housing	
Material	gold-coated molybdenum
Gaps Electrodes/Test mass	4 mm (x), 2.9 mm (y), 3.5 mm (z)
Electrodes	
Material	gold-coated sapphire
Size and Arrangement	see figure 16

*5.3.3. Launch lock and repositioning* The relatively large gaps make it necessary that the test mass is held fixed during launch by the *caging mechanism* to avoid damage to the test mass or the electrode housing due to the vibrations present during launch. During launch lock, eight hydraulically actuated fingers connect to the eight corners of the cubical test mass, each pushing with a force of 1200 N to keep the test mass securely in place (see figure 14, lower left panel for a drawing of the caging mechanism).

Releasing the test mass from the launch lock requires to break the adhesion present between the fingers and the surface of the test mass. The necessary force to break the adhesion can be up to 10 N per finger (on the order of 1 % of the load), so that without a way to push the test mass off the fingers, it would remain stuck to the launch lock. In addition, the residual momentum of the test mass after release needs to be smaller than  $10^{-5}$  N s for the electro-static actuator to be able to slow down and centre the test mass in the electrode housing.

A multi-stage approach for the release of the test mass has been taken: To overcome the adhesion between the fingers and the test mass, two piezo-driven plungers, acting centrally on the  $+Z$  and  $-Z$  surface of the test mass, respectively, are used to push the test mass off the fingers. The  $Z$  surfaces of the test mass have pyramidal/conical indentations to allow for an auto-centring and auto-aligning of the test mass during engagement of the plungers (see figure 14, upper left panel).

As the plungers push with up to 40 N into the indentations, an adhesion force of about 0.5 N will have to be overcome when attempting to retract the plungers. For that purpose, the plungers accommodate a release tip at their end (much like a retractable ball-point pen) that can be pushed out by a piezo-electric element to deliver the necessary force. The remaining adhesion, still too large to be overcome by the electro-static actuator [98], is then broken using the inertia of the test mass by quickly retracting the plunger, leaving the test mass with residual momentum below the specified  $10^{-5}$  N s.

After launch, only the plungers are employed to grab and position the test mass during spacecraft safe mode or any other circumstance that makes it necessary to re-position the test mass.

The breaking of the adhesion between plungers and test mass has been the topic of intense ground-based testing, showing the feasibility of a test mass release within the required limits of the transferred momentum [99].

*5.3.4. Vacuum system* It is a peculiarity of LISA (and LISA Pathfinder) that despite the fact that the mission will operate in interplanetary space, it needs to carry a vacuum system. The residual gas pressure due to outgassing in the inertial sensor is too high for the gravitational reference sensor to tolerate, as it creates spurious noise due to the radiometric effect [86] and through gas damping. Therefore, a vacuum system (figure 17), pumped by a getter pump and encapsulating the test mass, the electrode housing and ancillary structures is foreseen, maintaining a pressure of  $10^{-8}$  mbar. Due to the criticality of ferro-magnetic materials that close to the test masses, this vacuum system has been made entirely from titanium.

*5.3.5. Charge control system* As forcing of the test mass depend to a large degree on electrostatic forces, the electric charge of the test mass has to be controlled as any fluctuation in the charge of the test mass will give rise to a fluctuation in force, hence acceleration noise.

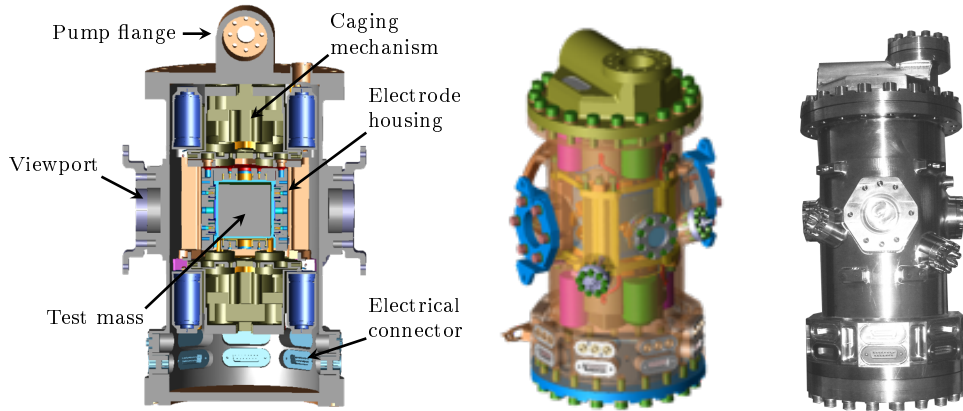


**Figure 17.** Left: Schematic drawing of the vacuum housing for the inertial sensor of LISA Pathfinder. Centre: Schematic drawing, external view. Right: Flight model of the vacuum housing for the inertial sensor of LISA Pathfinder. The inertial sensor for LISA is foreseen to be identical to the sensor used in LISA Pathfinder.

Charging of the test mass mainly occurs when secondary particles created by interaction of either protons or  $\alpha$ -particles from cosmic radiation with the spacecraft materials hit the test mass [100, 101]. The charging rates incurred are on the order of  $50 e/s$ .

A standard way to discharge test masses in similar setups is to connect a thin wire of conductive material to the test mass [102], however, such a mechanical connection introduces spurious accelerations and proves to be too noisy for the LISA requirements. Another well proven way to remove surface charge is through the photo-electric effect. In the case of LISA, UV light will be used to irradiate test mass and electrode housing, removing surface charges from electrodes and test mass.

The charge control system for LISA is based on heritage from the LISA Pathfinder mission [103], which itself is based on the charge control system flown on the GP-B mission, and whose functionality and performance of the discharging system has been demonstrated [104]. The LISA Pathfinder charge control system consists of six mercury discharge lamps, producing UV light at 254 nm coupled into optical fibres and brought to the test mass (2 lamps) and electrode housing (1 lamp). An identical setup controls the charge of the second test mass, bringing the number of lamps up to the total of six.

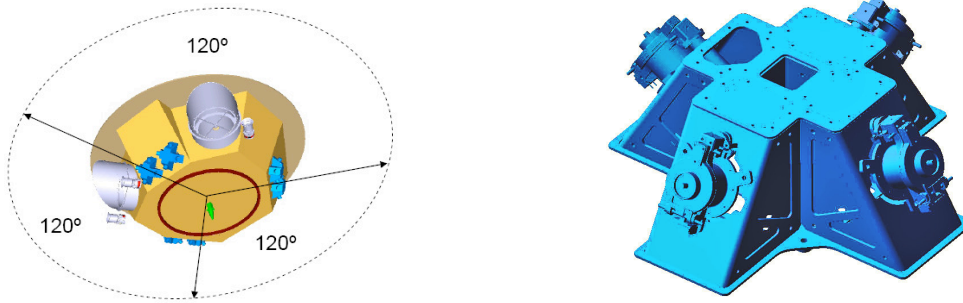
Due to the reflectivity of both the electrodes and the test mass, light shone on any surface will eventually reach most of the other surfaces as well and release electrons, so that the discharge rate is determined by the net current between electrodes and test mass. The polarity of the discharge is controlled by the digitally controlled output power of the UV lamps received by the test mass and the electrode housing, respectively, and can be further controlled by applying bias voltages to the electrodes.

Operationally, the discharging can occur episodic or continuously, depending on the observed charge rate. The charge itself is measured by applying an AC voltage to the electrodes and measure the ensuing displacement of the test mass [101, 103].

For LISA the development of UV LED [105] opens the possibility to replace the mercury discharge lamps with LED requiring less power and having less mass.

**Table 7.** Summary of the micro-Newton thruster requirements.

	Requirement
Minimum thrust	0.3 $\mu\text{N}$
Maximum thrust	100 $\mu\text{N}$
Thrust resolution	0.3 $\mu\text{N}$
Thrust noise	$0.1 \mu\text{N} \sqrt{\text{Hz}}^{-1} \times \sqrt{1 + \left(\frac{10 \text{ mHz}}{f}\right)^4}$
Lifetime	55 000 hours
Specific impulse	4000 s
Total impulse	8300 N s per thruster

**Figure 18.** Geometrical layout of the micro-newton thrusters on the LISA spacecraft (left) and FEEP cluster module geometry (right). Drawing courtesy of EADS Astrium

#### 5.4. Micro-newton thrusters

The micro-newton thrusters are a key technology for LISA, as they are providing the fine attitude and position control for the drag free flight. LISA will employ three clusters of four thrusters each, situated on the outside of the spacecraft, separated by  $120^\circ$  (see figure 18, allowing to control all degrees of freedom of the spacecraft).

The thrusters are controlled by the DRS and operate continuously during science operation. The main thrust is used to counteract the solar radiation pressure that amounts to about  $10 \mu\text{N}$  per relevant thruster, the largest external force on the spacecraft. The thrust noise is required to be smaller than  $0.1 \mu\text{N}$  at high frequencies (relaxing to lower frequencies, see table 7) in order to keep the motion of the spacecraft with respect to the test masses as small as possible.

Two different propulsion systems currently meet the LISA requirements on thrust and thrust noise, both based on field emission ionisation of the propellant. A colloid micro-newton thruster (CMNT) developed in the US and the European field emission electric propulsion system (FEEP). Both thruster systems will be flown on LISA Pathfinder [21] to demonstrate the technology and to assess the on-orbit performance.

The US CMNT uses a colloidal liquid as a propellant. Small droplets of the colloid are ionised through field emission, accelerated in an electrical field and ejected from the thruster. The thrust is over a wide range proportional to the acceleration voltage and can be controlled with the required precision. The CMNT has shown a capability of  $15 \mu\text{N}$  thrust with a noise well below the requirement and has successfully passed a

3400 hour life time test.

The ESA FEEP development programme advanced two different technologies, based on indium [106–110] and caesium [111] with different geometrical setups for the field emission. The advantage over the CMNT lies in the much higher specific impulse of the FEEP, as single ions instead of charged droplets are accelerated and ejected, yielding a better charge to mass ratio.

In the In-FEEP capillary forces push the indium to the tip of a needle where it is ionised, whereas the Cs-FEEP employ a narrow slit in which the caesium then forms narrow cones due to the electric field, emitting ions from the tip of the cones, producing higher thrust than the In-FEEP due to the multiple emitters.

The Cs-FEEP have been chosen as the baseline technology to fly on LISA PF and have demonstrated the required thrust, noise and resolution and have performed endurance testing with a total impulse in excess of 800 Ns in over 3000 hours of operation; a campaign to measure the thrust directly on a nano-balance is ongoing, aimed at verifying the thrust measurements obtained from monitoring the electrical current produced by the thrusters.

While the currently demonstrated lifetime and total impulse of both micro-newton thruster systems is sufficient for the LISA Pathfinder mission, a higher lifetime and total impulse has to be demonstrated for LISA. The additional life-time testing is part of ESA's technology development programme for LISA.

## 6. Conclusions

LISA is the first space mission dedicated to gravitational waves and will deliver a rich scientific payoff. The technology that is employed by LISA has seen significant advances in the last couple of years, not least to the technology development programme for the technology precursor mission LISA Pathfinder.

The main technology areas of LISA are the interferometric measurement system, comprising the laser, the telescope, the optical bench and the phase measurement; and the disturbance reduction system, consisting of the gravitational reference sensor with test mass, housing and caging mechanism, the control law, and the micro-Newton thrusters.

LISA can claim significant heritage from LISA Pathfinder in the DRS, where almost all of the technologies will be flight-tested during the LPF mission: the gravitational reference sensor, the micro-newton thrusters, and the charge-control system. While the control law requires adaptation due to the different mass and moments of inertia of LISA and due to the fact the LISA has to keep two test masses in free fall condition, the principle of a drag-free control system able to operate at the required levels of noise will be demonstrated.

The technology needed for the interferometric measurements benefits less from the LPF mission, however, important issues such as the construction of an ultra-stable optical bench and the design principles of the interferometer are part of the technology that LPF will demonstrate.

The remaining technology items, such as the phase measurement for LISA, the telescope, and the high power laser system are subject to an ongoing technology programme conducted by ESA and NASA as well as the participating national space agencies.

## 7. Acknowledgement

The author would like to thank P McNamara, G Heinzl, W Weber and D Nicolini for providing many details on the technology and useful feedback, K Danzmann and S Vitale for helpful comments, and EADS Astrium GmbH, in particular D Weise and P Gath, for providing high-quality graphics for the optical bench, the optical assembly and the micro-propulsion system.

## References

- [1] Johann UA et al. 2008 The European Space Agency's LISA mission study: status and present results *Journal of Physics: Conference Series* **122**, 012005
- [2] Stebbins R, Merkowitz SM and Livas JC 2006 LISA Mission Tutorial *Proc. 6th Int. LISA Symp.* Vol. 873 (Greenbelt, Maryland (USA): AIP), pp. 3–12
- [3] Danzmann K 2003 LISA - An ESA cornerstone mission for the detection and observation of gravitational waves *Advances in Space Research* **32**, 1233–1242
- [4] Bender P et al. LISA – Laser Interferometer Space Antenna for the detection and observation of gravitational waves **208** Max-Planck-Institut für Quantenoptik, 1996
- [5] Hough J 2007 Long baseline gravitational wave detectors – status and developments *Journal of Physics: Conference Series* **66**, 012002
- [6] Sigg D and the LIGO Science Collaboration 2006 Status of the LIGO detectors **23**, S51–S56
- [7] Willke B and the LIGO Science Collaboration 2007 GEO600: status and plans *Class. Quantum Grav.* **24**, S389–S397
- [8] Acernese F et al. 2006 The status of VIRGO *Class. Quantum Grav.* **23**, S63–S69
- [9] Shoemaker D 2003 Ground-based interferometric gravitational-wave detectors in the LISA epoch **20**, S12–S21
- [10] Ando M and the TAMA Collaboration 2002 Current status of TAMA *Class. Quantum Grav.* **19**, 1409–1419
- [11] Robertson NA 2000 Laser interferometric gravitational wave detectors *Class. Quantum Grav.* **17**, R19–R40
- [12] Menou K, Haiman Z and Kocsis B 2008 Cosmological physics with black holes (and possibly white dwarfs) *New Astronomy Reviews* **51**, 884–890
- [13] MacLeod CL and Hogan CJ 2008 Precision of Hubble constant derived using black hole binary absolute distances and statistical redshift information *Phys. Rev. D* **77**, 043512–8
- [14] Deffayet C and Menou K 2007 Probing Gravity with Spacetime Sirens *Astrophys. J.* **668**, L143–L146
- [15] Amaro-Seoane P et al. 2007 TOPICAL REVIEW: Intermediate and extreme mass-ratio inspirals – astrophysics, science applications and detection using LISA *Class. Quantum Grav.* **24**, 113–+
- [16] Hogan CJ 2006 Gravitational Wave Sources from New Physics *Proc. 6th Int. LISA Symp.* Vol. 873 (Greenbelt, Maryland (USA): AIP), pp. 30–40

- [17] Holz DE and Hughes SA 2005 Using Gravitational-Wave Standard Sirens *ApJ* **629**, 15–22
- [18] Berti E, Buonanno A and Will CM 2005 Testing general relativity and probing the merger history of massive black holes with LISA *Class. Quantum Grav.* **22**, S943–S954
- [19] Folkner WM et al. 1997 LISA orbit selection and stability *Class. Quantum Grav.* **14**, 1405–1410
- [20] Misner CW, Thorne KS and Wheeler JA 1973 *Gravitation* (W. H. Freeman), p. 1215
- [21] McNamara P, Vitale S and Danzmann K 2008 LISA Pathfinder *Class. Quantum Grav.* **25**, 114034
- [22] Armano M et al. 2009 LISA Pathfinder: the experiment and the route to LISA *Classical and Quantum Gravity* **26**, 094001–+
- [23] Lang RN and Hughes SA 2008 Localizing Coalescing Massive Black Hole Binaries with Gravitational Waves *Astrophys. J.* **677**, 1184–1200
- [24] Lang RN and Hughes SA 2006 Measuring coalescing massive binary black holes with gravitational waves: The impact of spin-induced precession *Phys. Rev. D* **74**, 122001–+
- [25] Larson SL, Hiscock WA and Hellings RW 2000 Sensitivity curves for spaceborne gravitational wave interferometers *Phys. Rev. D* **62**, 062001–+
- [26] Heinzel G et al. 2003 Interferometry for the LISA technology package (LTP) aboard SMART-2 *Class. Quantum Grav.* **20**, S153–S161
- [27] Haberland R Flexure joint, particularly for connecting a gyroscope to its driving shaft U.S. Patent No. 4261211 U.S. Classification: 74/5F; 267/160; 308/2A ; International Classification: G01C 1922 1981
- [28] Middleton KF et al. 2006 Prototype optical bench instrument in the interferometer for the LISA–Pathfinder space mission *Optical Engineering* **45**, 125601–11
- [29] Braxmaier C et al. 2004 LISA pathfinder optical interferometry *Gravitational Wave and Particle Astrophysics Detectors* vol. 5500 (Glasgow, Scotland, United Kingdom: SPIE), pp. 164–173
- [30] Killow CJ et al. 2006 Construction of the LTP Optical Bench Interferometer *Proc. 6th Int. LISA Symp.* Vol. 873 (Greenbelt, Maryland (USA): AIP), pp. 297–303
- [31] Turneaure JP et al. 2003 Development of the Gravity Probe B flight mission *Advances in Space Research* **32**, 1387–1396
- [32] Gwo DH 1998 Ultraprecision bonding for cryogenic fused-silica optics vol. 3435, pp. 136–142
- [33] Amico P et al. 2002 Fused silica suspension for the VIRGO optics: status and perspectives *Class. Quantum Grav.* **19**, 1669–1674
- [34] Smith JR et al. 2003 Mechanical loss associated with silicate bonding of fused silica *Class. Quantum Grav.* **20**, 5039–5047
- [35] Elliffe EJ et al. 2005 Hydroxide-catalysis bonding for stable optical systems for space *Class. Quantum Grav.* **22**, S257–S267

- [36] Zawischa I et al. 1999 All-solid-state neodymium-based single-frequency master-oscillator fiber power-amplifier system emitting 5.5 W of radiation at 1064 nm *Optics Letters* **24**, 469–471
- [37] Weßels P, Auerbach M and Fallnich C 2002 Narrow-linewidth master oscillator fiber power amplifier system with very low amplified spontaneous emission *Optics Communications* **205**, 215–219
- [38] Bartelt-Berger L et al. 2001 Space qualified ultra stable laser source *Lasers and Electro-Optics, 2001. CLEO '01. Technical Digest. Summaries of papers presented at the Conference on*, pp. 580–581
- [39] Roth A and Werninghaus R 2006 Status of the TerraSAR-X Mission *Geoscience and Remote Sensing Symposium, 2006. IGARSS 2006. IEEE International Conference on*, pp. 1918–1920
- [40] Sodnik Z, Furch B and Lutz H 2006 Free-Space Laser Communication Activities in Europe: SILEX and beyond *Lasers and Electro-Optics Society, 2006. LEOS 2006. 19th Annual Meeting of the IEEE*, pp. 78–79
- [41] Livas JC, Thorpe JI and Numata K 2007 Tunable Frequency-stabilized Lasers for LISA vol. 211, p. 990
- [42] Thorpe JI, Numata K and Livas JC Laser frequency stabilization and control through offset sideband locking to optical cavities *Optics Express to be published*
- [43] Mueller G et al. Laser frequency stabilization for LISA Technical Report **NASA/TM-2005-212794; Rept-2006-00387-1** Document ID: 20060012084 Goddard Space Flight Center, 2005, p. 23
- [44] Leonhardt V and Camp JB 2006 Space interferometry application of laser frequency stabilization with molecular iodine *Applied Optics* **45**, 4142–4146
- [45] Leonhardt V et al. 2006 Iodine laser frequency stabilization for LISA *Proc. 6th Int. LISA Symp.* Vol. 873 (Greenbelt, Maryland (USA): AIP), pp. 354–358
- [46] Wand V et al. 2006 Noise sources in the LTP heterodyne interferometer *Class. Quantum Grav.* **23**, S159–S167
- [47] Heinzl G et al. 2006 Interferometry for the LISA technology package LTP: an update *Journal of Physics: Conference Series* **32**, 132–136
- [48] Notcutt M et al. 2005 Simple and compact 1-Hz laser system via an improved mounting configuration of a reference cavity *Optics Letters* **30**, 1815–1817
- [49] Nevsky AY et al. 2001 Frequency comparison and absolute frequency measurement of I<sub>2</sub>-stabilized lasers at 532 nm *Optics Communications* **192**, 263–272
- [50] Hong FL et al. 1998 Portable I<sub>2</sub>-stabilized Nd:YAG laser for wavelength standards at 532 nm and 1064 nm vol. 3477, pp. 2–10
- [51] Musha M et al. 2000 The short- and long-term frequency stabilization of an injection-locked Nd:YAG laser in reference to a Fabry-Perot cavity and an iodine saturated absorption line *Optics Communications* **183**, 165–173
- [52] Mondin L et al. 2004 Validation of a laser source for gravitational wave space detectors *Journal de Physique IV* **119**, 237–238
- [53] Chang DH et al. 2007 Waveguide PPLN second harmonic generator for NASA's space interferometry mission (SIM) *Nanophotonics and Macrophotonics for Space Environments* vol. 6713 (San Diego, CA, USA: SPIE), 67130U–13

- [54] Sheard BS et al. 2003 Laser frequency stabilization by locking to a LISA arm *Physics Letters A* **320**, 9–21
- [55] Sylvestre J 2004 Simulations of laser locking to a LISA arm *Phys. Rev. D* **70**, 102002
- [56] Herz M 2005 Active laser frequency stabilization and resolution enhancement of interferometers for the measurement of gravitational waves in space *Optical Engineering* **44**
- [57] Marín AFG et al. 2005 Phase locking to a LISA arm: first results on a hardware model *Class. Quantum Grav.* **22**, S235–S242
- [58] Thorpe JI et al. 2006 Arm-Locking in a LISA-like Hardware Model: A Status Report vol. 873, pp. 661–667
- [59] Shaddock DA et al. 2004 Postprocessed time-delay interferometry for LISA *Phys. Rev. D* **70**, 081101–+
- [60] Giampieri G et al. 1996 Algorithms for unequal-arm Michelson interferometers *Opt. Commun.* **123**, 669–678
- [61] Tinto M and Armstrong JW 1999 Cancellation of laser noise in an unequal-arm interferometer detector of gravitational radiation *Phys. Rev. D* **59**, 102003
- [62] Armstrong JW, Estabrook FB and Tinto M 1999 Time-Delay Interferometry for Space-Based Gravitational Wave Searches *Astrophys. J.* **527**, 814–826
- [63] Cornish NJ and Hellings RW 2003 The effects of orbital motion on LISA time delay interferometry *Class. Quantum Grav.* **20**, 4851–4860
- [64] Tinto M, Estabrook FB and Armstrong JW 2002 Time-delay interferometry for LISA *Phys. Rev. D* **65**, 082003
- [65] Shaddock DA et al. 2003 Data combinations accounting for LISA spacecraft motion *Phys. Rev. D* **68**, 061303
- [66] Dhurandhar SV, Nayak KR and Vinet JY 2002 Algebraic approach to time-delay data analysis for LISA *Phys. Rev. D* **65**, 102002
- [67] Nayak KR and Vinet JY 2004 Algebraic approach to time-delay data analysis for orbiting LISA *Phys. Rev. D* **70**, 102003
- [68] Dhurandhar SV, Vinet JY and Nayak KR 2008 General relativistic treatment of LISA optical links *0805.4314*
- [69] Romano JD and Woan G 2006 Principal component analysis for LISA: The time delay interferometry connection *Phys. Rev. D* **73**, 102001–7
- [70] Dhurandhar SV and Tinto M 2005 Time-Delay Interferometry *Living Reviews in Relativity* **8**
- [71] Cruz RJ et al. 2006 The LISA benchtop simulator at the University of Florida *Class. Quantum Grav.* **23**, S751–S760
- [72] Cruz RJ et al. 2006 Time Delay Interferometry using the UF LISA Benchtop Simulator *Proc. 6th Int. LISA Symp.* Vol. 873 (Greenbelt, Maryland (USA): AIP), pp. 319–325
- [73] Heinzl G et al. 2004 The LTP interferometer and phasemeter *Class. Quantum Grav.* **21**, S581–S587
- [74] Jennrich O et al. 2001 Demonstration of the LISA phase measurement principle *Class. Quantum Grav.* **18**, 4159–4164

- [75] Pollack SE and Stebbins RT 2006 Demonstration of the zero-crossing phasemeter with a LISA test-bed interferometer *Class. Quantum Grav.* **23**, 4189–4200
- [76] Pollack SE and Stebbins RT 2006 A demonstration of LISA laser communication *Class. Quantum Grav.* **23**, 4201–4213
- [77] Shaddock D et al. 2006 Overview of the LISA Phasemeter *Proc. 6th Int. LISA Symp.* Vol. 873 (Greenbelt, Maryland (USA): AIP), pp. 654–660
- [78] Armano M et al. 2005 Gravitational compensation for the LISA pathfinder *Class. Quantum Grav.* **22**, S501–S507
- [79] Brandt N et al. 2005 LISA Pathfinder E2E performance simulation: optical and self-gravity stability analysis *Class. Quantum Grav.* **22**, S493–S499
- [80] Merkowitz SM et al. 2004 Structural, thermal, optical and gravitational modelling for LISA *Class. Quantum Grav.* **21**, S603–S610
- [81] Merkowitz SM et al. 2005 Self-gravity modelling for LISA *Class. Quantum Grav.* **22**, S395–S402
- [82] Weber WJ et al. 2002 Position sensors for LISA drag-free control *Class. Quantum Grav.* **19**, 1751–1756
- [83] Carbone L et al. 2003 Achieving Geodetic Motion for LISA Test Masses: Ground Testing Results *Physical Review Letters* **91**, 151101
- [84] Stanga R et al. 2006 Ground Based 2 DoF Test For LISA And LISA Pathfinder: A Status Report *Proc. 6th Int. LISA Symp.* Vol. 873 (Greenbelt, Maryland (USA): AIP), pp. 210–214
- [85] Carbone L et al. 2005 Characterization of disturbance sources for LISA: torsion pendulum results *Class. Quantum Grav.* **22**, S509–S519
- [86] Carbone L et al. 2007 Thermal gradient-induced forces on geodesic reference masses for LISA *Phys. Rev. D* **76**, 102003–21
- [87] Shaul DNA et al. 2005 Evaluation of disturbances due to test mass charging for LISA *Class. Quantum Grav.* **22**, S297–S309
- [88] Shaul DNA et al. 2004 Unwanted, coherent signals in the LISA bandwidth due to test mass charging *Class. Quantum Grav.* **21**, S647–S651
- [89] Everitt CWF et al. 2008 Gravity Probe B data analysis status and potential for improved accuracy of scientific results *Class. Quantum Grav.* **25**, 114002
- [90] Weber W et al. 2007 Possibilities for measurement and compensation of stray DC electric fields acting on drag-free test masses *Advances in Space Research* **39**, 213–218
- [91] Dolesi R et al. 2003 Gravitational sensor for LISA and its technology demonstration mission *Class. Quantum Grav.* **20**, S99–S108
- [92] Carbone L et al. 2006 Torsion pendulum facility for direct force measurements of LISA GRS related disturbances *Proc. 6th Int. LISA Symp.* Vol. 873 (Greenbelt, Maryland (USA): AIP), pp. 561–565
- [93] Hueller M et al. 2005 Measuring the LISA test mass magnetic properties with a torsion pendulum *Class. Quantum Grav.* **22**, S521–S526

- [94] Budworth DW, Hoare FE and Preston J 1960 The Thermal and Magnetic Properties of Some Transition Element Alloys *Proceedings of the Royal Society of London. Series A, Mathematical and Physical Sciences (1934-1990)* **257**, 250–262
- [95] Silvestri Z et al. 2003 Volume magnetic susceptibility of gold-platinum alloys: possible materials to make mass standards for the watt balance experiment *Metrologia* **40**, 172–176
- [96] Carbone L et al. 2007 Upper limits to surface-force disturbances on LISA proof masses and the possibility of observing galactic binaries *Phys. Rev. D* **75**, 042001–6
- [97] Cavalleri A et al. 2001 Progress in the development of a position sensor for LISA drag-free control *Classical and Quantum Gravity* **18**, 4133–4144
- [98] Benedetti M et al. 2006 The Influence of Adhesion and Sub-Newton Pull-Off Forces on the Release of Objects in Outer Space *Journal of Tribology* **128**, 828–840
- [99] Borotoluzzi D et al. 2009 LISA Pathfinder test mass injection in geodesic motion: status of the on-ground testing *Class. Quantum Grav.*
- [100] Jafry Y and Sumner TJ 1997 Electrostatic charging of the LISA proof masses *Class. Quantum Grav.* **14**, 1567–1574
- [101] Sumner T et al. 2004 Description of charging/discharging processes of the LISA sensors *Class. Quantum Grav.* **21**, S597–S602
- [102] Touboul P et al. 1996 Electrostatic accelerometers for the equivalence principle test in space *Class. Quantum Grav.* **13**, A67–A78
- [103] Schulte M et al. 2006 The Charge-Management System on LISA-Pathfinder — Status & Outlook for LISA *Proc. 6th Int. LISA Symp.* Vol. 873 (Greenbelt, Maryland (USA): AIP), pp. 165–171
- [104] Wass PJ et al. 2006 Testing of the UV discharge system for LISA Pathfinder *Proc. 6th Int. LISA Symp.* Vol. 873 (Greenbelt, Maryland (USA): AIP), pp. 220–224
- [105] Sun KX et al. 2006 LED deep UV source for charge management of gravitational reference sensors *Class. Quantum Grav.* **23**, S141–S150
- [106] Genovese A et al. 2004 New Generation of Clusterable In-FEEP Emitters vol. 555, p. 29
- [107] Tajmar M, Genovese A and Steiger W 2004 Indium Field Emission Electric Propulsion Microthruster Experimental Characterization *Journal of Propulsion and Power* **20**, 211–218
- [108] Steiger W, Genovese A and Tajmar M 2000 Micronewton Indium FEEP thrusters vol. 465, p. 475
- [109] Fehringer M, Ruedenauer F and Steiger W 1998 Indium Liquid-Metal Ion Sources as Micronewton Thrusters vol. 456, pp. 207–213
- [110] Ruedenauer GF, Fehringer M and Steiger W 1997 Indium Field Emission Microthrusters vol. 398, p. 267
- [111] Marcuccio S, Genovese A and Andrenucci M 1998 Experimental Performance of Field Emission Microthrusters *Journal of Propulsion and Power* **14**, 774–781